

## Research Paper

## Regenerative cooling in hybrid rocket engines based on Self-Pressurized liquid nitrous oxide

Giuseppe Gallo<sup>1,\*</sup>, Yuta Miyahara<sup>2</sup>, Landon Kamps<sup>3</sup>, Harunori Nagata<sup>4</sup>*Hokkaido University, Sapporo, Hokkaido 060-8628, Japan*

## A B S T R A C T

An experimental investigation of the reliability and feasibility of a regenerative cooling system in hybrid rocket engines based on saturated nitrous oxide is presented. The novelty of the work consists in the use of a cooling system based on saturated liquid nitrous oxide, wrapping the external surface of a COTS graphite nozzle. The detrimental heat fluxes developed at the throat are handled with a slight increase in assembly complexity. Ten firing tests are performed with an incremental logic of the mass flow rate from 9 to 45 g/s, which is controlled by cavitating the fluid through orifices with different diameters upstream of the cooling system. The tests have been performed at different ambient temperatures in different seasons. The multiphase state of the coolant is evaluated by measuring pressure and temperature upstream and downstream of the cavitation orifice and cooling channels. The test with the smallest mass flow rate developed the highest vapour fraction downstream of the orifice and cooling channels at 0.458 and 0.481, respectively. The cooling performance is indirectly evaluated by measuring the nozzle temperature at 3, 5, and 8.5 mm from the throat internal surface. The results show that steady temperatures are achieved inside the nozzle, with throat temperatures included between 700 and 1200 K in a chamber pressure range between 5 and 30 bar. Nozzle erosion never occurs in the entire experimental campaign, and the nozzles are totally reusable for more ignitions. The coolant heat transfer coefficient increased from 3912 to 21181 W/(m<sup>2</sup>•K) by increasing the flow rate per channel from around 3 to 15 g/s. Compared to cryogenic oxygen, liquid nitrous oxide displays higher cooling performance. Finally, the cavitation orifice is moved downstream of the cooling system, showing worse performance of the overall propulsion system.

## 1. Introduction

Due to the many advantages they can offer for space propulsion applications, hybrid rockets (HREs) became popular among the rocket society. The combination of safety and simplicity is the primary characteristic of hybrid rockets [1,2,3]. Hybrid rockets are green and compatible with human health [4,5]. However, their simplicity introduces intrinsic drawbacks, such as low capability to handle detrimental heat fluxes developed in the nozzle. Most developers opt not to use active cooling systems for the nozzle throat, relying on carbon-based materials for thermal protection. However, graphite nozzles are extremely sensitive to hot oxidizer-rich flows, and they can exhibit throat erosion [6]. Nozzle erosion concerns the degradation and regression of the inner surface of a carbon-based nozzle as a result of chemical reactions with the combustion gas [7,8]. Two ingredients are required for the occurrence of nozzle erosion: combustion products rich in oxidizing species and high temperatures at the nozzle throat [9,10]. While it is impossible to control the species produced by combustion,

cooling the nozzle below the erosion activation temperature could be the solution for this phenomenon.

Even when nozzle erosion is not experienced, thermal issues may be encountered with rocket motors working in deep space. Because no heat transfer mechanisms are available with the ambient in addition to radiation, the heat fluxes developed at the nozzle could rise up to the satellite payload and bus by the spacecraft structure [11]. In the case of no active cooling, large and heavy thermal protection systems (TPS) are used for the nozzle thermal insulation [12]. In the authors' experience, TPS weight could increase close to 50 % of the overall propulsion system. Therefore, regenerative cooling improves the density-specific impulse of the propulsion system by discouraging nozzle erosion and reducing the total mass.

Differently from liquid rocket engines, hybrid rockets work with solid fuels accommodated in the combustion chamber, and the oxidizer is only available in the liquid phase [13]. Refrigeration by oxidizers in rocketry is uncommon because of their limited cooling capabilities [14,15,16]. In addition, propellants in HREs work in subcritical conditions, since high chamber pressures are not required. Therefore, the

\* Corresponding author.

E-mail address: [gallo@eng.hokudai.ac.jp](mailto:gallo@eng.hokudai.ac.jp) (G. Gallo).

<sup>1</sup> JSPS International Fellow, Department of Mechanical and Space Engineering.

<sup>2</sup> Master Student, Department of Mechanical and Space Engineering.

<sup>3</sup> Adjunct Associate Professor, Department of Mechanical and Space Engineering.

<sup>4</sup> Professor, Department of Mechanical and Space Engineering.

## Nomenclature

$A$	= area, $\text{m}^2$
$c_p$	= specific heat at constant pressure, $\text{J}/(\text{kg}\cdot\text{K})$
$D$	= diameter, $\text{m}$
$D_h$	= hydraulic diameter, $\text{m}$
$e_k$	= kinetic energy, $\text{J}/\text{kg}$
$f$	= skin friction coefficient
$G$	= mass flux, $\text{kg}/(\text{m}^2\cdot\text{s})$
$h$	= heat transfer coefficient, $\text{W}/(\text{m}^2\cdot\text{K})$
$hs$	= sensible enthalpy, $\text{J}/\text{kg}$
$k$	= thermal conductivity, $\text{W}/(\text{m}\cdot\text{K})$
$L$	= length, $\text{m}$
$m$	= mass flow rate, $\text{g}/\text{s}$
$M_f$	= fuel mass, $\text{kg}$
$M_w$	= molecular weight
$N_{ch}$	= channel number
$OF$	= mixture ratio
$p$	= pressure, bar
$\dot{Q}_x$	= heat flux per unit of length, $\text{W}/\text{m}$
$\dot{Q}_v$	= vaporization heat, $\text{J}/\text{kg}$
$s$	= entropy, $\text{J}/(\text{kg}\cdot\text{K})$
$t_b$	= burning time, $\text{s}$
$T$	= temperature, $\text{K}$
$T_h$	= thrust, $\text{N}$
$u$	= velocity, $\text{m}/\text{s}$
$X$	= vapour quality
$y$	= radial coordinate

## Greek Symbols

$\alpha$	= void fraction
$\Delta$	= jump
$\mu$	= viscosity, $\text{kg}/(\text{m}\cdot\text{s})$
$\rho$	= density, $\text{kg}/\text{m}^3$
$\epsilon$	= measurement error

## Superscripts

$\sim$	= time average
$-$	= time average

## Subscripts

$1$	= upstream of cavitation orifice
$2$	= upstream of cooling system
$3$	= downstream of cooling system
$c$	= coolant
$ch$	= channel
$ext$	= external
$f$	= fuel
$g$	= gaseous
$h$	= hot
$l$	= liquid
$m$	= mixture
$n1$	= 3 mm from the throat
$n2$	= 5 mm from the throat
$n3$	= 8.5 mm from the throat
$ox$	= oxidizer
$t$	= throat
$tot$	= total
$v$	= vapour
$w$	= wall

## Acronyms

$A$	= autumn
$S$	= summer
$W$	= winter
$NC$	= no cooling
$HDPE$	= high-density polyethylene
$HRE$	= hybrid rocket engine
$LOX$	= liquid oxygen
$TPS$	= thermal protection system

cooling benefits of the supercritical state are also missing, and unpredictable operations related to multiphase flows and coolant boiling might be experienced. However, our innovative concept consists of cooling classic graphite nozzles, whose onset erosion temperature is over 1400 K [17]. Because the maximum allowable temperature of graphite is higher than other materials, such as copper, excellent cooling performance is not required, making oxidizers a good candidate for this application. An additional advantage of using an ablative material is the redundant safety; simply put, cooling a graphite nozzle throat increases the safety and reliability of the system because the risk of catastrophic failure in the case of anomalous overheating, etc., is mitigated down to a risk of minor performance loss resulting from nozzle erosion.

These aspects have been recently investigated by the authors. Several experimental tests and numerical studies have been performed in the past years on a 30 N hybrid rocket engine equipped with regenerative cooling based on cryogenic oxygen (LOX) in helical channels. A preliminary design carried out by a one-dimensional numerical model displayed the capability of regenerative cooling to suppress nozzle erosion and suggested the optimum number of channels in terms of pressure drop and heat absorbed per unit of mass flow rate [18]. A successive extensive campaign consisting of eight firing tests using LOX/HDPE highlighted the benefits and drawbacks of using regenerative cooling in hybrid rockets [19]. In contrast to firing tests without cooling, nozzle erosion was never experienced, and the throat temperature was limited to a steady value between 700 and 800 K. The main observed con was the lower test repeatability and predictability due to the large coolant gasification. The coolant boiling mainly controlled the pressure

jump along channels and the cooling performance. The most critical temperatures at the throat were achieved when coolant dry-out was reached.

The novelty of this work is the use of saturated liquid nitrous oxide ( $\text{LN}_2\text{O}$ ) as a coolant and oxidizer for regenerative cooling in HREs. The cooling capability and phase change of  $\text{LN}_2\text{O}$  are experimentally characterized by a series of firing tests. We are interested in  $\text{LN}_2\text{O}$  because it is storable and self-pressurized at room temperature due to the vapour pressure (i.e., 55.5 atm at 25 °C) [20,21]. However, it is extremely dangerous to use as a coolant, since it can decompose when a sufficient local high temperature is achieved [22,23,24].

The heat transfer from the hot nozzle surface to the multiphase nitrous oxide mixture flowing inside the cooling channels is the main thermal process investigated in the paper. To the authors' knowledge, four previous works are only available in the inherent literature, exploring  $\text{LN}_2\text{O}$  as a coolant for propulsive applications. Regenerative cooling in bipropellant lab-scale motors using ethylene or ethane and additionally boosted by extra cooling with  $\text{LN}_2\text{O}$  have been investigated in Ref. [25,26]. Regarding HREs, a feasibility study on the cooling of HRE nozzles using supercritical nitrous oxide was carried out in Ref. [27]. Nevertheless, the pioneering work in Ref. [28] is the most relevant work; in fact, it also explored the possibility of using saturated  $\text{LN}_2\text{O}$  for throat cooling in a HRE through an experimental campaign including six firing tests. However, our concept is different in several aspects, motivated by our intention to drastically reduce the cost and complexity of regenerative cooling manufacturing and assembly with the thrust chamber:

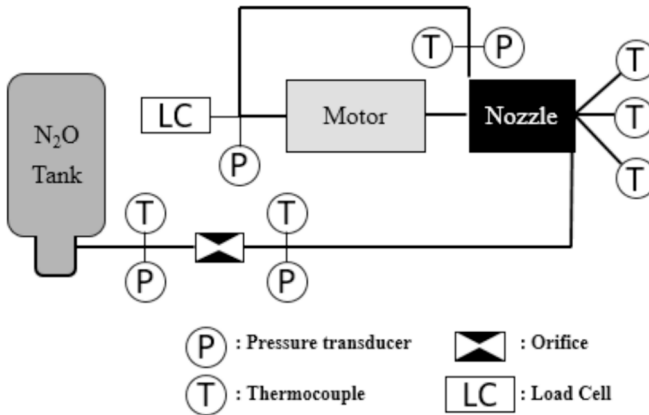


Fig. 1. Schematic of the facility used for the experimental tests.

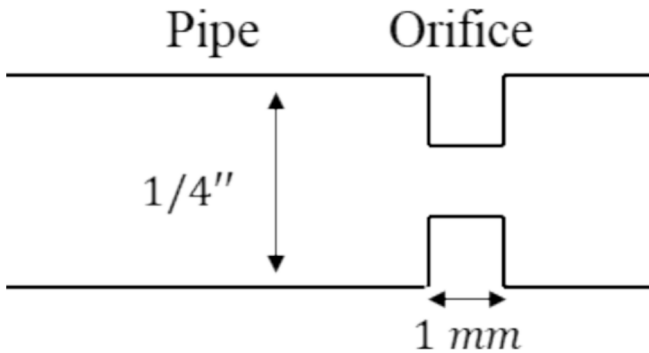


Fig. 2. Sketch of the cavitation orifice. The orifice diameter changes with the target mass flow rate.

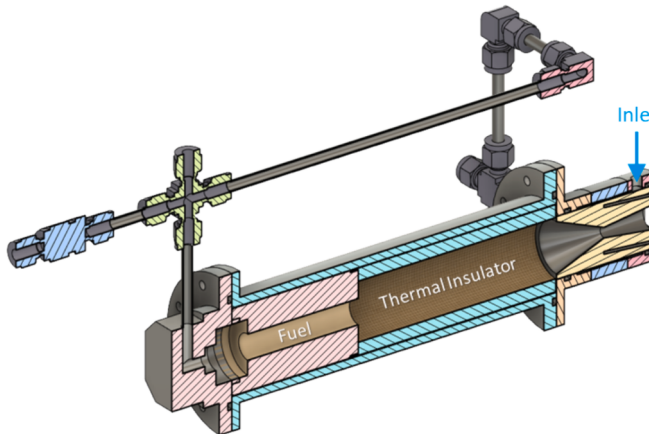


Fig. 3. Motor schematic.

1. The nozzle used in the current work is a classic graphite nozzle of HREs because of the above-mentioned reasons. In the referenced work, the nozzle was metallic with a copper insert at the throat.
2. Our cooling system is made up of three helical channels that cover the external nozzle surface. Therefore, the cooling channels are placed significantly far from the throat. In the referenced work, the cooling system was simply a single annular channel placed next to the internal surface of the throat.

Different operating conditions have been investigated by increasing the mass flow rate step by step from 8 to 45 g/s. The cooling performance has been indirectly calculated by temperatures measured inside

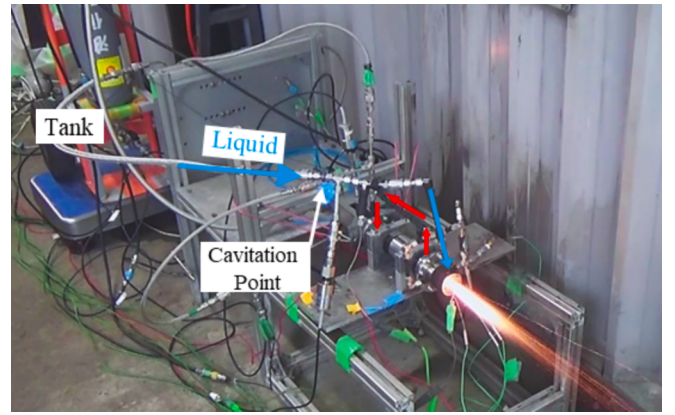


Fig. 4. Picture of the hybrid rocket motor: the blue and red arrows represent the path of the cold and hot coolant, respectively. (For interpretation of the references to colour in this figure legend, the reader is referred to the web version of this article.)

the nozzle and compared with data on cryogenic oxygen from our previous experimental campaign.

The work consists of three main sections. Firstly, the experimental set-up is described, including the data reduction techniques used to calculate the most interesting heat transfer and multiphase quantities, such as the cooling heat transfer coefficient, the coolant vapour quality, and the void fraction. Secondly, the data collected in the experimental campaign is shown and discussed with a focus on the capability of regenerative cooling to suppress nozzle erosion, increase nozzle reliability, and limit temperatures. Finally, the cooling performance in terms of pressure jump and heat transfer of liquid nitrous oxide is displayed and compared with cryogenic oxygen, highlighting the effect of the coolant phase state at the channels' inlet.

## 2. Experimental setup and data reduction technique

This section describes the test apparatus and the hybrid rocket motor configuration. Fig. 1 shows a simplified diagram of the experimental facility employed for the firing tests. The fuel and the oxidizer employed in the firing tests were HDPE and LN<sub>2</sub>O, respectively. Because of the self-pressure capability of LN<sub>2</sub>O, the setup is drastically simplified compared to our previous one used for LOX. The setup starts with the tank, which is turned upside down in order to supply N<sub>2</sub>O in the liquid phase. It is directly connected to the cavitation orifice by a flexible pipe, whose geometry is represented in Fig. 2. The coolant is directly supplied to the channels' inlet, and the channels' outlet is connected to the motor inlet by a rigid pipe system displayed in Fig. 3. Pressure transducers and thermocouples are installed upstream and downstream of the orifice, the cooling system, and the motor inlet. The motor case is connected to the load cell by a dedicated trapezoidal support. Summing up, the following path is taken by the coolant: firstly, the LN<sub>2</sub>O is cavitated through an orifice for mass flow rate regulation; secondly, the multiphase coolant is injected into helical channels to cool the graphite rocket nozzle; finally, it is injected into the main combustion chamber. LN<sub>2</sub>O is pushed into the feeding line by the vapour pressure achieved in the tank at room temperature.

No pressurizing system is involved in the experimental set-up; consequently, the coolant upstream pressure is sensitive to the ambient conditions. We performed tests in summer, autumn, and winter with a room temperature decrease from 299 to 279 K. As shown in the results, the season (or the ambient temperature) affects the tank pressure, which drops from 58 to 35 bar. Therefore, to obtain the same mass flow rate, a smaller cavitation orifice is required in the summer than in the winter in order to provide a larger pressure drop; consequently, the vapour fraction developed by cavitation in summer is higher compared

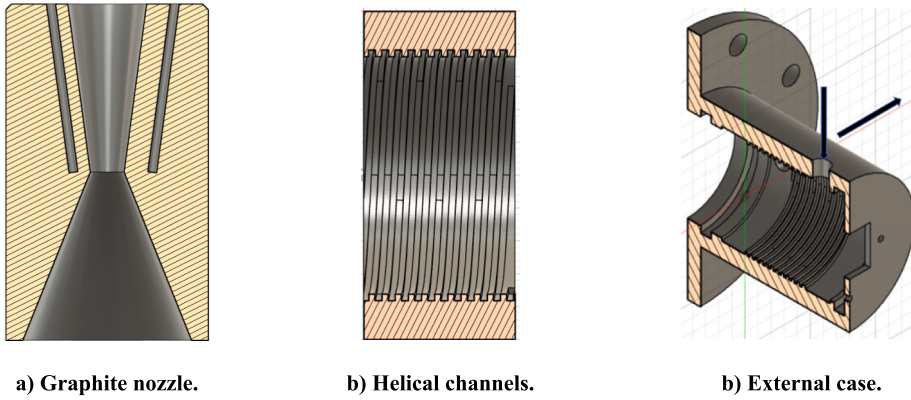


Fig. 5. Details of graphite nozzle insert and the metallic case.

to a test performed in winter with the same mass flow rate. This effect on the cooling performance is discussed in the experimental results. An additional nitrogen tank is included in the mainline for motor purging. The liquid nitrous oxide tank was placed above a scale for the measurement of the mass loss of the reservoir during the burning time.

The same motor configuration as in the previous experimental campaign performed with cryogenic oxygen is used in the current campaign (see Fig. 3). The motor length is optimized to achieve the optimum OF condition of the couple O<sub>2</sub>/HDPE around 2.5. The objective of this campaign is to demonstrate the cooling capability of nitrous oxide in the worst thermal conditions. For this reason, the fuel length was reduced from 220 to 90 mm, and the remaining length was replaced with Bakelite thermal insulation. This configuration ensures harsh oxidizer-rich combustion products and a long residence time for the combustion gas. Indeed, the mixture ratio of the tests is between 7 and 10 with a combustion efficiency close to unity.

Fig. 4 shows a representation of the experimental set-up and the concept of regenerative cooling. The cold oxidizer coming from the pressurized tank flows through a cavitation orifice. The mass flow rate is regulated by the orifice diameter. Smaller diameters provide larger gasification, and then lower flow rates. The multiphase mixture is supplied inside the cooling system, which consists of three helical channels wrapped around the external diameter of the graphite nozzle. The pressure and temperature are recorded upstream and downstream of the orifice, downstream of the cooling system, and just before the combustion chamber. Because no injector is used, it is assumed that the last pressure coincides with the chamber one. The pressure is measured with three Kyowa PHB-A transducers with an instrument measurement error of  $\pm 1 \cdot 10^4$  Pa. The temperature is measured by a thermocouple of K-type with an error of  $\pm 2.5$  K. Furthermore, the rocket is placed in front of a Kyowa LMB-A-50 N class load cell for the measurement of the thrust with an error of  $\pm 0.30$  N. The time-averaged oxidizer mass flow rate is obtained by the time derivative of the linear best fit of the measured tank mass during the burning time, whose mass is obtained with an error of  $\pm 45$  g. The analogue signals generated by thermocouples, pressure transducers, and load cells are sampled at 200 Hz, digitally converted, processed, and recorded on the hard disk by a Kyowa universal recorder EDX-100A standard system interconnected with the computer by means of fiber optic connections. Finally, the fuel consumption, essential for the evaluation of the average mixture ratio and the characteristic velocity, is estimated by measuring the fuel grain weight before and after the firing test on a digital scale with an error of  $\pm 1$  g.

A graphite nozzle is used in the tests, which is provided with three holes for inserting sheath-type thermocouple leads, by which nozzle temperatures were measured at 3, 5, and 8.5 mm from the inside surface of the throat section. The nozzles used in all tests were manufactured using the same grade of isotropic graphite (G347; Tokyo Tokai Carbon, Ltd.). The density and thermal conductivity at atmospheric conditions

are listed by the manufacturer to be  $\rho_n = 1850$  kg/m<sup>3</sup> and  $k = 116$  W/(m·K), respectively [29]. The nozzle length is 60 mm, and the throat is located in the middle. The convergent inlet section, the throat, and the exit section have a diameter of 30 mm, 6 mm, and 14 mm, respectively. The external diameter (around which the channels are wrapped) is 36 mm. The nozzle is mounted within a metallic case containing three helical fins with a width and height of 1 mm, which travel around the nozzle axis with a rotation angle of around 3 degrees. The nozzle length featured by helical channels is 24 mm, placed symmetrically with the throat. The channels have been manufactured by a metal 3D printer; the current channels' dimensions represent the lower manufacturing limit of the printer. Therefore, three helical channels are obtained from the accommodation of the nozzle into the metallic case. The choice of the number of channels was deeply discussed in our previous work [18]. The coolant flows in the opposite direction from the exhausting gases. The heated coolant is gathered in a collector at the channels' end and injected into the main chamber by a pipe system. Fig. 5 represents the described assembly.

The evaluation of the nozzle erosion is performed using image techniques. Initial and final nozzle throat diameter measurements were taken by analysing digital photographs of the nozzle before and after firing using ImageJ [30]. These photographs were taken at 40X digital zoom from a distance of 2 m from the nozzle throat. A length scale was established for the scan by placing a plaque of 1-mm-spacing grid paper next to the nozzle being scanned. This procedure was repeated five times before and after each firing test, and the standard deviation of these measurements was incorporated into the uncertainty of this measurement; however, the standard deviation of measurements was typically much smaller than the uncertainty of the length scale. The length scale uncertainty was assumed to be two times the thickness of a grid line (0.2 mm).

## 2.1. Data reduction technique

### 2.1.1. Propulsion, multiphase and heat transfer quantities

In this subsection, all the equations used for the calculation of the main quantities from the measured ones are shown. First, the burning time has been computed, starting from half of the pressure rise to half of the final pressure drop. From the fuel grain mass loss and the burning time, the average fuel mass flow, mixture ratio, and characteristic velocity can be calculated as

$$\begin{aligned}\widetilde{\dot{m}_f} &= \frac{\Delta M_f}{t_b} \\ \widetilde{OF} &= \frac{\dot{m}_{ox}}{\widetilde{\dot{m}_f}} \\ \widetilde{c}^* &= \frac{p_e A_t}{\dot{m}_{ox} + \widetilde{\dot{m}_f}}\end{aligned}\quad (1)$$

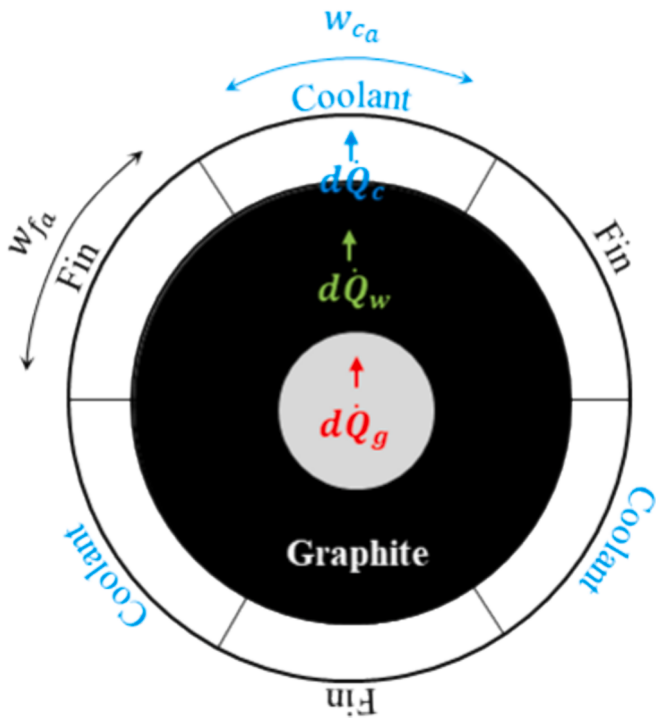


Fig. 6. Schematic of heat transfer path from hot gases to cooling channels.

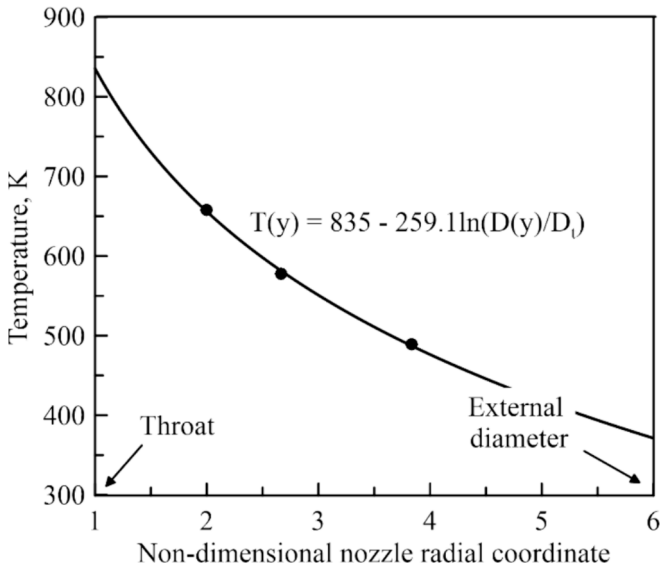


Fig. 7. A representation of a typical experimental temperature profile along the nozzle thickness at the throat.

Two main pressure and temperature jumps, i.e. pressure and temperature differences, are observed in the experimental set-up: the first through the cavitation orifice and the second through the cooling system. Because the coolant pressure and temperature are known upstream and downstream of these segments, the outlet mixture conditions can be evaluated by considering an energy jump equation. The equation for the cavitation orifice is easier because this element is not heated, and we can neglect the heat exchanged from the coolant with the ambient. For the cavitation orifice, assuming:

1. No slip conditions between the liquid and gaseous phase;
2. Both phases have the same temperature;

3. The vapour and liquid thermodynamic properties coincide with the saturated ones;

The outlet vapour quality,  $X_2$ , is given by:

$$(1 - X_1)hs_{l,1} + X_1hs_{v,1} + \frac{G^2}{2\rho_{m,1}^2} = (1 - X_2)hs_{l,2} + X_2hs_{v,2} + \frac{G^2}{2\rho_{m,2}^2} \quad (2)$$

where  $hs$  is the sensible enthalpy,  $G$  is the mass flux, and  $\rho_m$  is the mixture density. The notations 1 and 2 indicate the coolant properties upstream and downstream of the cavitation orifice,  $l$  and  $v$  indicate the liquid and vapour phases, respectively. Note that the inlet vapour quality,  $X_1$ , for the cavitation orifice is equal to 0, since the coolant is supplied in liquid state, ensured by the upside tank flip. In the case of cooling channels, additional assumptions are introduced in subsection 3.3.2 for a rough estimation of the coolant gas fraction at the channels' exit. The void fraction, mixture density, and specific heat are evaluated as:

$$\begin{aligned} \alpha &= \frac{X\rho_l}{X\rho_l + (1 - X)\rho_v} \\ \rho_m &= \alpha\rho_v + (1 - \alpha)\rho_l \\ \mu_m &= \alpha\mu_v + (1 - \alpha)\mu_l \\ c_{p_m} &= Xc_{p_v} + (1 - X)c_{p_l} \end{aligned} \quad (3)$$

Regarding the evaluation of the heat transfer quantities at the throat, the methodology used for the evaluation of the coolant heat transfer coefficient,  $h_c$ , the hot gas heat transfer coefficient,  $h_g$ , and the heat flux per unit of length,  $\dot{Q}_x$ , is described. Heat is transferred from the hot-gas (subscript  $g$ ) to the coolant (subscript  $c$ ) via the solid wall of the graphite nozzle, as shown in Fig. 6.

The one-dimensional model relies on the heat transfer balance between hot gas, wall, and coolant for steady-state conditions. The hot-gas heat transfer rate by convection affects the wall ( $\dot{Q}_{g,x}$ ), is transmitted by conduction through the wall ( $\dot{Q}_{w,x}$ ), and is transported by convection to the coolant ( $\dot{Q}_{c,x}$ ). For steady-state conditions, these heat transfer rates must be equal:

$$\dot{Q}_x = \dot{Q}_{g,x} = \dot{Q}_{w,x} = \dot{Q}_{c,x} \quad (4)$$

where  $\dot{Q}_x$  is the heat transfer rate per unit of length. At the steady state in correspondence of the throat section, the terms in the above heat balance equation are given by:

$$\dot{Q}_{g,x} = \pi D_t h_g (T_0 - T_{wh}) \quad (5)$$

where  $D_t$  is the throat diameter,  $T_{wh}$  is the nozzle temperature at the throat from the hot side, while  $T_0$  is the adiabatic wall temperature, which coincides with the flame temperature assuming a unitary recovery factor. As displayed in the next sections, the vapour quality at the outlet of the cooling system is lower than 0.5 in any test. For the sake of simplicity, the flame temperature is calculated by chemical equilibrium calculations assuming liquid nitrous oxide and high density polyethylene (HDPE) at the corresponding average mixture ratio. Note that  $h_g$ , evaluated by Eq.(5), also includes uncertainty regarding the deviation of the experimental temperature from the equilibrium combustion one corresponding to the experimental average mixture ratio. On the coolant side, the heat equation is given by:

$$\dot{Q}_{c,x} = \frac{\pi D_{ext}}{2} h_c (T_{wc} - T_c) \quad (6)$$

where  $D_{ext}$  is the external nozzle diameter,  $T_{wc}$  is the nozzle temperature at the coolant side, while  $T_c$  is the coolant temperature at the throat, which is assumed equal to  $\bar{T}$  of Eq.(3). It is worth noticing that the wet surface  $\pi D_{ext}$  is divided by 2 in order to take into account the presence of

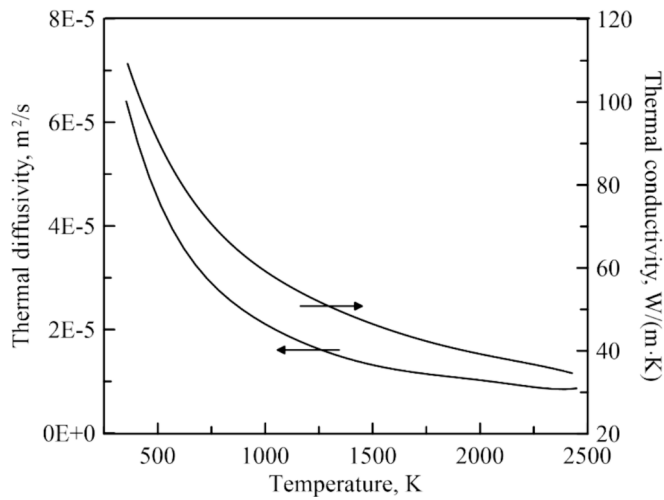


Fig. 8. Graphite thermal properties with density equal to  $1850 \text{ kg/m}^3$ .

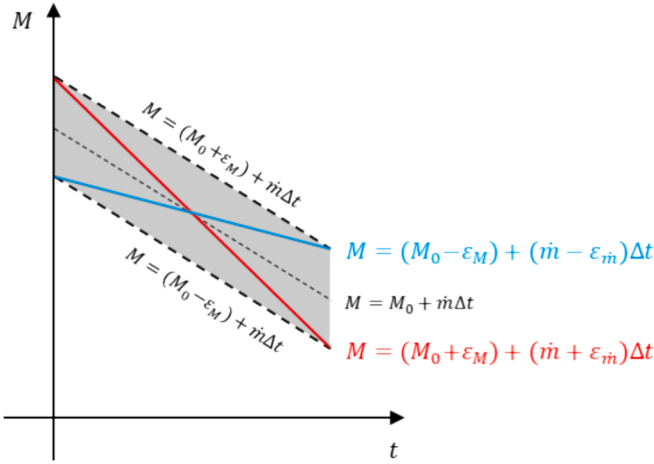


Fig. 9. Sketch of the error measurement of the mass flow rate.

the fins, as displayed in Fig. 6. This is true, assuming that the lateral walls of the channel are adiabatic.

Regarding the heat conduction through the solid nozzle, the 1D Fourier's law of heat conduction for heat transfer through a cylindrical layer with non-negligible thickness is expressed as

$$\dot{Q}_{w,x} = \frac{2\pi k_s(T)}{\ln(D_{ext}/D_t)} (T_{wh} - T_{wc}) \quad (7)$$

where  $k_s$  is the graphite thermal conductivity, which, in turn, depends on the nozzle temperature. Therefore, from Eq.(7) the following

expression can be obtained

$$T(y) = T_{wh} - \frac{\dot{Q}_x}{2\pi k_s(T)} \ln(D(y)/D_t) \quad (8)$$

where  $y$  is the nozzle radial coordinate at the throat. Let us give an example of how to use Eq.(8). As stated above, the nozzle temperatures are recorded at 3, 5 and 8.5 mm from the throat; hence the corresponding non-dimensional diameters,  $D(y)/D_t$ , are equal to 2, 2.67, 3.83, respectively. Plotting the steady state temperatures against the non-dimensional diameters and computing the logarithmic best-fit trend-line, an equation similar to Eq.(8) can be obtained. In the

**Table 2**  
Nozzle temperatures measured at 3, 5 and 8.5 mm from the throat inner surface.

Test	Nozzle temperature at 3 mm, $T_{n1}$ , K	Nozzle temperature at 5 mm, $T_{n2}$ , K	Nozzle temperature at 8.5 mm, $T_{n3}$ , K
1 W	594	550	478
2 W	629	550	480
3 W	658	578	489
4A	610	564	489
5A	607	555	475
6S	478	455	441
7S	601	560	491
8S	694	625	559
9S	886	729	675
10S	800	770	573

**Table 3**  
Motor operating conditions.

Test	Coolant mass flow rate, $\tilde{m}_c$ , g/s	Mixture ratio, $\tilde{OF}$	Chamber pressure, $\tilde{p}_{ch}$ , bar	Thrust, $\tilde{T}_h$ , N	Characteristic velocity, $\tilde{c}^*$ , m/s
1 W	16.0 ± 1.19	9.18 ± 0.77	10.00	30.22	1592 ± 107
2 W	18.2 ± 1.25	10.64 ± 0.85	10.61	35.55	1505 ± 95
3 W	22.1 ± 1.24	12.91 ± 0.88	12.52	45.17	1485 ± 77
4A	11.7 ± 1.17	9.46 ± 1.06	7.03	19.63	1535 ± 139
5A	15.5 ± 1.23	9.66 ± 0.87	9.51	26.65	1571 ± 114
6S	8.8 ± 1.24	9.64 ± 1.32	5.42	15.44	1576 ± 203
7S	13.2 ± 1.24	7.17 ± 0.73	8.50	22.08	1597 ± 132
8S	20.0 ± 1.28	9.79 ± 0.72	11.98	34.68	1535 ± 89
9S	26.3 ± 1.33	9.36 ± 0.55	15.55	51.95	1509 ± 69
10S	45.1 ± 1.46	9.01 ± 0.36	28.04	105.61	1581 ± 46

**Table 1**

Pressure cascade and temperatures measured upstream and downstream of the cavitation orifice and cooling system.

Test	Orifice upstream pressure, $p_1$ , bar	Orifice upstream temperature, $T_1$ , K	Cooling upstream pressure, $p_2$ , bar	Cooling upstream temperature, $T_2$ , K	Cooling downstream pressure, $p_3$ , bar	Cooling downstream temperature, $T_3$ , K
1 W	35.11	279	16.20	251	11.81	243
2 W	38.70	283	19.78	258	12.89	258
3 W	35.09	279	21.05	260	14.72	251
4A	45.14	287	12.16	245	9.72	289
5A	45.18	287	16.08	248	12.04	265
6S	57.92	299	10.55	239	6.87	300
7S	57.86	299	17.12	253	10.80	318
8S	57.90	299	22.41	262	14.28	296
9S	57.80	299	31.14	273	19.37	310
10S	57.85	299	44.08	286	31.31	274

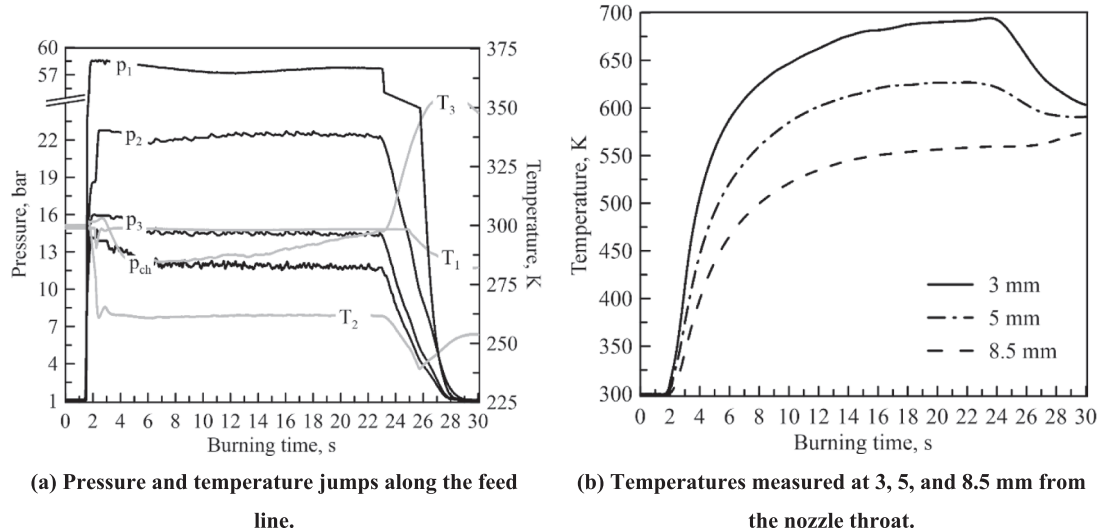


**Fig. 10.** A representation of the operative conditions in Test 8S during the burning time.

particular case of Fig. 7, the equation is

$$T(y) = 835 - 259.1 \ln(D(y)/D_t) \quad (9)$$

where:

- $T_{wh}$  is immediately evaluated, and it is equal to 835 K;
- $T_{wc}$  is around 376 K, and it is obtained by evaluating the regression law at  $D(y)/D_t$  equal to 6;
- $\dot{Q}_c$  is assessed by multiplying 259.1 by  $2\pi k(T)$ . The thermal conductivity of the graphite was evaluated at the average temperature of the radial profile. The dependence of the graphite properties on temperature is taken into account following Ref. [31], whose profile of thermal diffusivity and conductivity are shown in Fig. 8.

Once obtained these three quantities,  $h_g$  and  $h_c$  are given by Eq. (5) and Eq. (6).

The error of the quantities directly measured, such as pressure, temperature, and thrust, coincides with the error of the pressure transducers, thermocouples, and the load cell. The error of the quantities computed by elementary operations (addition, subtraction, division, and multiplication) is evaluated by the propagation error formulas [32]. On the other hand, a different approach is used for the quantities evaluated by trendlines of experimental values, such as mass flow rate, temperature at the inner throat surface, and heat exchanged at the throat. For instance, the mass flow rate is obtained by measuring the mass of the tank during the burning time, which is affected by an error,  $\varepsilon_M$ . Therefore, the tank mass during the burning time is included in the black box displayed in Fig. 9. The major and minor diagonals represent the over- and under-estimated mass flow rate, thus the positive and negative error of the measured quantity of the mass flow rate, indicated as  $\dot{m} \pm \varepsilon_m$ . The methodology sketched in Fig. 9 can be extended to any quantity derived from any kind of trend line (linear, logarithmic, power, etc.).

### 3. Experimental results

This section presents the main experimental findings of the test campaign. It has been organized in the following way:

1. Representation of a typical firing test and discussion of the collected data.
2. Effectiveness of regenerative cooling on nozzle erosion and thermal control.

3. Discussion of the pressure and temperature jumps by the cavitation orifice and cooling system.
4. Evaluation of the coolant state at each recorded station.
5. Representation of the cooling performance and comparison with cryogenic oxygen.
6. Effect of the cavitation orifice position.

#### 3.1. Typical experimental Test and measured results

The experimental campaign consists of ten firing tests performed at different coolant mass flow rates in a range between 8 and 45 g/s. Because the campaign was carried out during three different seasons, the tank pressure changed among the tests, increasing with the ambient temperature. Three data sets have been collected: Test 1 W, 2 W and 3 W have been performed in winter, Test 4A and 5A in autumn, and Test 6S, 7S, 8S, 9S and 10S in summer. The mass flow rate was regulated by the cavitation orifice, with different diameters included between 0.6 and 1.1 mm. To obtain the same mass flow rates, lower orifice diameters were required in the summer, during which the highest tank pressure of around 57 bar was reached at an ambient temperature of 299 K. The data in each dataset are ordered by increasing mass flow rates. The pressures and temperatures measured along the feed line and inside the nozzle are summed up in Table 1 and Table 2, while the motor operating conditions are in Table 3. The tank pressure decreased to around 45 and 35 bar in autumn and winter with an ambient temperature of 287 and 280 K, respectively. The pressure and temperature downstream of the orifice decreased with the mass flow rate from 44.08 to 10.55 bar and from 286 to 239 K for Test S, from 16.08 to 12.16 bar and from 248 to 245 K for Test A, and from 21.05 to 16.20 bar and from 260 to 251 K for Test W. The pressure downstream of the cooling system still decreases with the mass flow rate; nevertheless, a defined trend for the outlet temperature is not recognized in Table 1. The nozzle temperatures at 3, 5, and 8.5 mm from the throat inner surface range between 470 and 886 K, 455 and 770 K, and 441 and 675 K, respectively. The mixture ratio is mostly higher than the stoichiometric condition ( $OF = 8$ ), and it is between 7.17 and 12.91. The chamber pressure and thrust increase with the mass flow rate, from 5.42 to 28.04 bar and from 15.44 to 105.61 N.

Test 8S is described as a typical firing test of the presented experimental campaign. The labels 1, 2, and 3 indicate the quantity measured upstream of the orifice and upstream and downstream of the cooling system, respectively. Fig. 10a represents the pressure signals of  $p_1$ ,  $p_2$ ,  $p_3$ ,  $p_{ch}$  and the corresponding temperatures during the burning time. The self-pressure tank is able to supply the coolant in steady-state

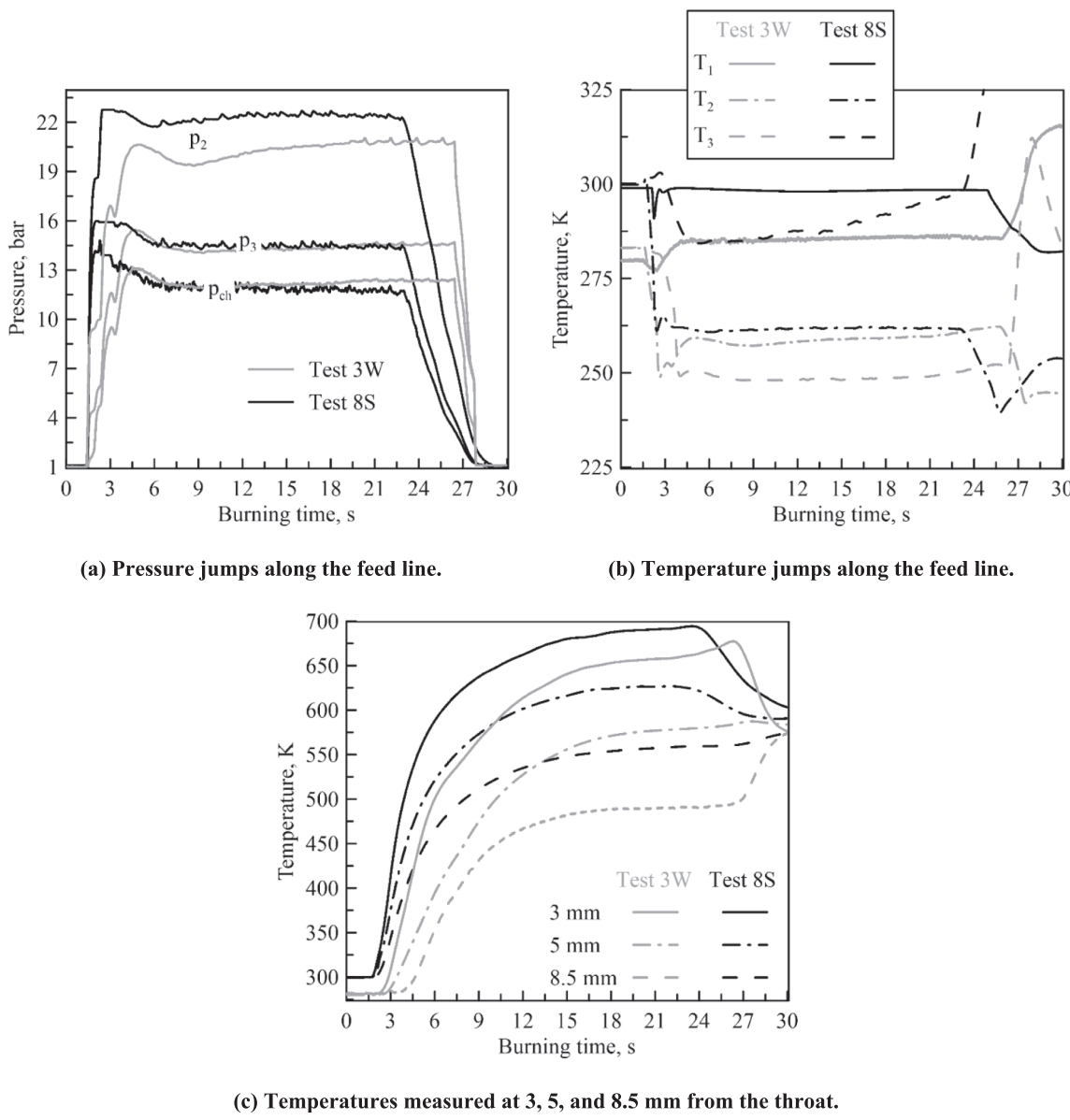
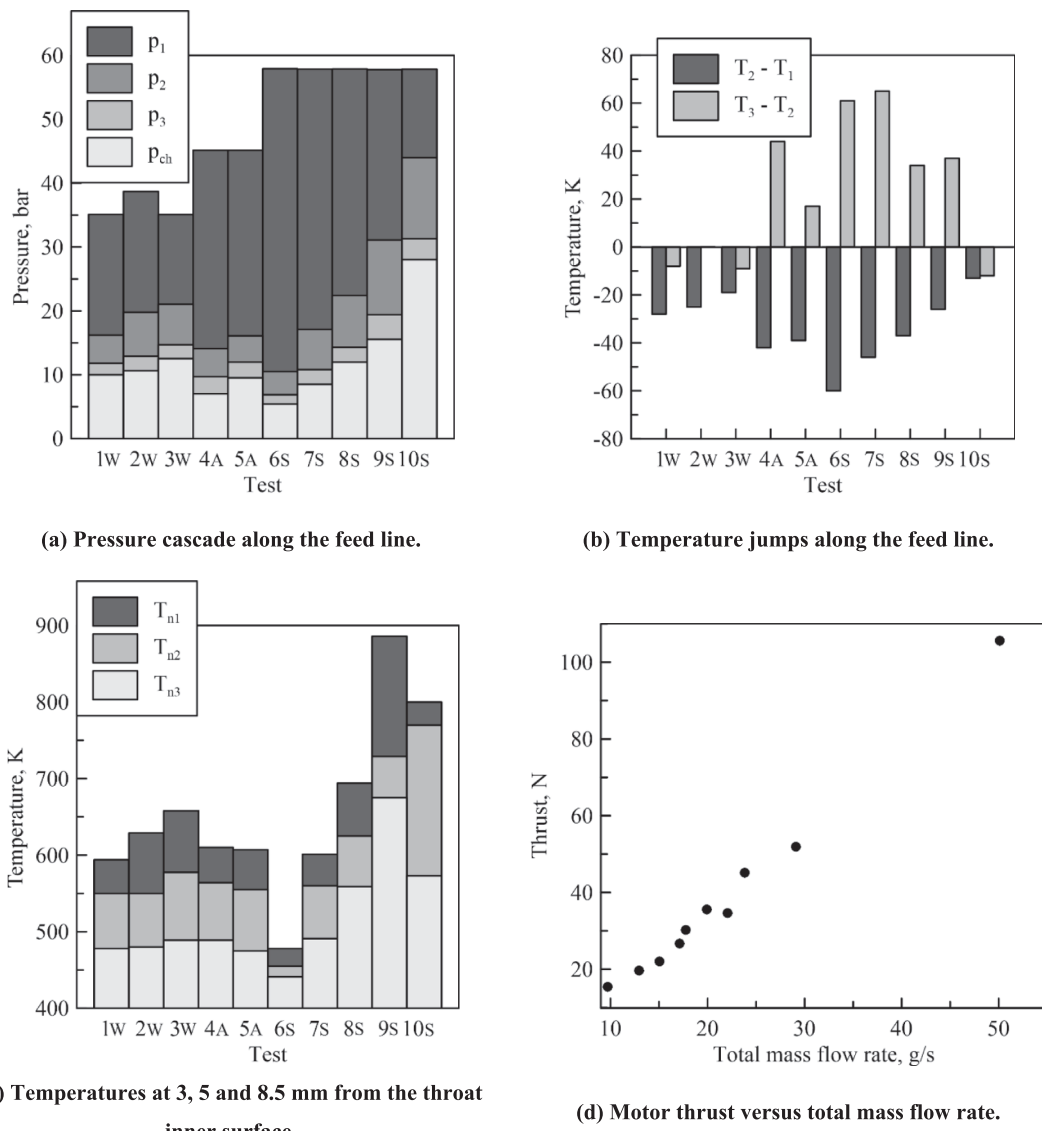


Fig. 11. Comparison of the operative conditions of Test 3 W with Test 8S.

conditions; indeed,  $p_1$  and  $T_1$  appear constant during the burning time. The overall fluidic system immediately reaches steady-state conditions. The largest pressure drop is observed through the cavitation orifice, with a drop of 34.59 bar. Then, the pressure decreases from 22.41 to 14.28 bar through the cooling channels and to 11.98 bar through the pipe system connecting the channels' outlet with the combustion chamber. Downstream of the orifice, the temperature drops from 299 to 262 K, and it is heated up along the cooling channels to 296 K. In this test, a perfect steady state condition of  $T_3$  is not reached with a total increment of 20 K at the end of the burning time. However, we considered this increment negligible compared with the temperature jumps observed in our previous experimental campaign with liquid oxygen, which were higher than 200 K. The outlet temperature of nitrous oxide is far from the activation temperature of  $\text{N}_2\text{O}$  thermal decomposition, which is usually higher than 1000 K.

Fig. 10b displays the temperatures measured along the nozzle thickness during the test. A sudden heating is observed in the first 10 s for all three thermocouples, which is damped by the cooling system and limited to steady-state values of 694, 625, and 559 K at 3, 5, and 8.5 mm from the throat, respectively.

Fig. 11 compares the operative conditions of Test 3 W and Test 8S, which are performed with the same mass flow rate of around 20 g/s with different  $p_1$  of 35 and 57 bar and different orifice diameters of 0.9 and 0.8, respectively. The pressure jumps through the cooling system are approximately 6 and 8 bar, respectively. An additional pressure jump of 2 bar is recorded between the outlet of the cooling system and the combustion chamber. Because the mass flow rate is the same in the two tests, the higher total jump ( $p_1 - p_{ch}$ ) of Test 8S suggests that the average coolant density in the feed system is lower than Test 3 W. This is further highlighted by  $T_3$  displayed in Fig. 11b. The temperature jump across the channels is positive in Test 8S and negative in Test 3 W, which indicates the higher gasification degree of the former test. Although  $T_1$  is higher in Test 8S,  $T_2$  is the same in both tests because of the different fluid expansion produced by the two different orifice diameters. Note that, although the pressure drops through the orifice are 20 and 35 bar in Test 3 W and 8S, respectively, the temperature drops are 19 K and 37 K due to the steep slope of the saturation vapour curve in the p-T diagram of nitrous oxide (additional discussions are provided in subsection 3.3). Finally, Fig. 11c displays a comparison of the nozzle temperatures achieved inside the nozzle. Although the thermal fields are comparable,



**Fig. 12.** A representation of the main quantities recorded in the experimental campaign.

the temperatures measured at 3, 5, and 8.5 mm are 40, 50, and 70 K lower than Test 8S, suggesting that the cooling performance is enhanced in Test 3 W.

Fig. 12 deeply represents all the main results collected among the tests. Fig. 12a shows the chain of pressure jumps recorded along the feed line. The most significant drop is observed through the cavitation orifice. Focusing on Tests S, the tank-to-chamber pressure ratio decreased from around 10 in Test 6S to 2 in Test 10S by increasing the orifice diameter from 0.6 to 1.1 mm with a corresponding increment of the mass flow rate from 8.8 to 45.1 g/s. Therefore, the mass flow rate is mainly controlled by the coolant cavitation through the orifice. Two additional drops proportional to the mass flow rate are observed through the cooling channels and the pipes connected to the combustion chamber.

Fig. 12b sums up the temperature jumps measured through the orifice and the cooling system. While the former are negative in any test, the latter are positive in all Tests A and S except for Test 10S. Comparing Fig. 12b with Fig. 12a, it can be noticed that the temperature difference,  $T_3 - T_2$ , is proportional to the pressure drop  $p_1 - p_2$ , suggesting that the gasification produced by the cavitation affects the temperature jump through the cooling channels. The outlet coolant temperature is far from the activation temperature of nitrous oxide decomposition in all the

tests.

Fig. 12c displays the temperatures achieved inside the nozzle. These significantly increase with the mass flow rate in Tests S, while they are restrained in a narrow range in all the other tests. The temperatures are dependent on the heat transferred from the combustion gas to the nozzle, the heat absorbed by the coolant from the nozzle surface, and the amount of steam developed by the coolant. Because both the gas and coolant heat transfer coefficients are related to the mass flow rate, the positive trend of nozzle temperatures with the mass flow rate in Tests S shows that the cooling system performance scales with the flow rate lower than the heat transferred from combustion gases. Nonetheless, nozzle erosion was never observed in any test, even in Test 10S, whose mass flow rate is definitely out of the design of this lab-scale motor.

Fig. 12d displays the motor thrust with the total mass flow rate, which linearly increases from 15 to 105 N with a mass flow rate of 9.7 to 50.11 g/s. The trend of the experimental characteristic velocity displayed in Fig. 12e is in line with the ideal characteristic velocity of liquid and gaseous nitrous oxide. In particular, the highest value is observed in Test 7S, with a characteristic velocity equal to 1597 m/s at  $OF = 7$ .

Fig. 12f displays the pressure jump through the orifice divided by the square of the mass flow rate versus the orifice diameter. The ratio

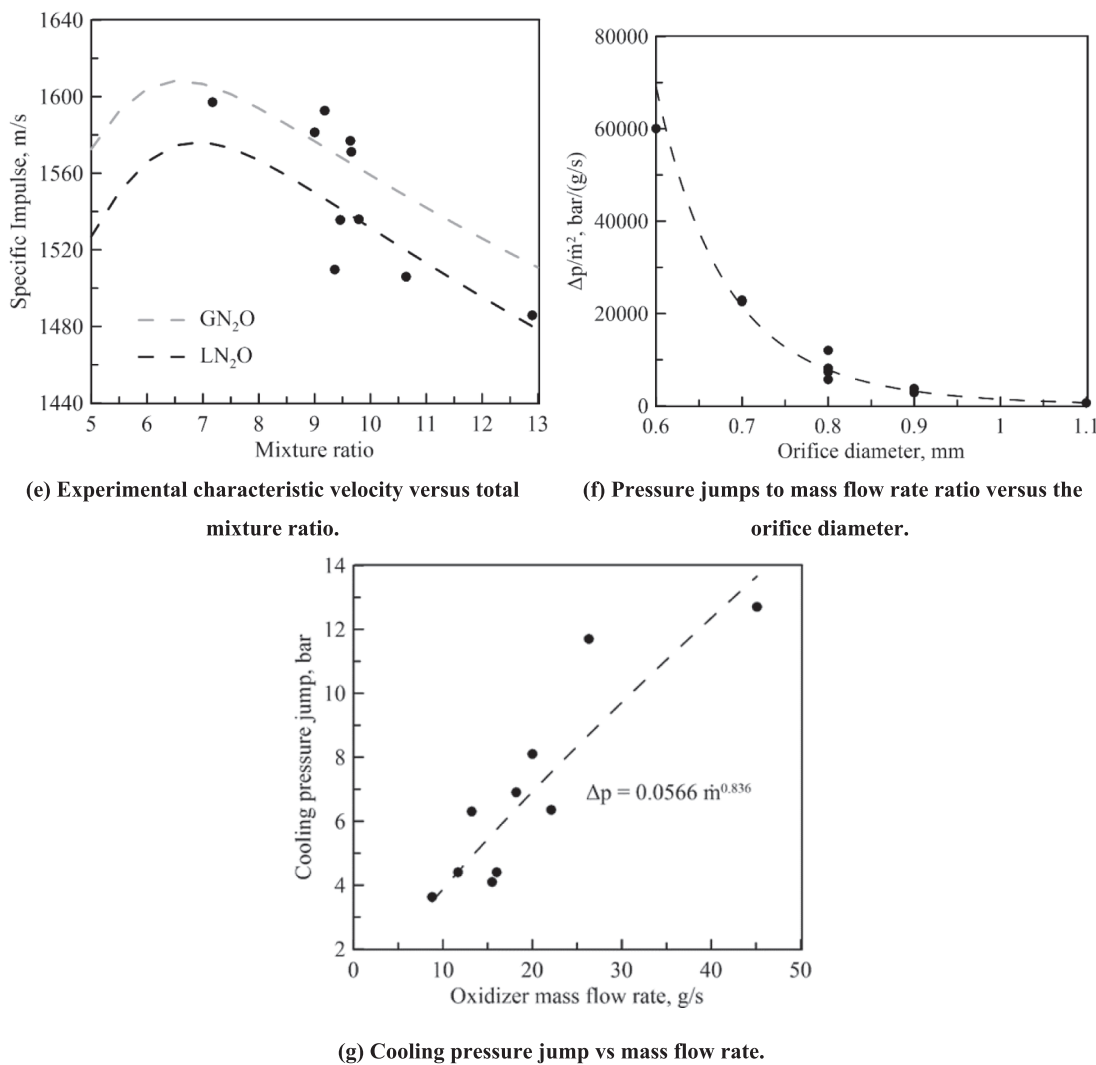


Fig. 12. (continued).

**Table 4**  
Operative conditions of Test NC.

Test	Coolant mass flow rate, g/s	Mixture ratio	Chamber pressure, bar	Thrust, N	Characteristic velocity, m/s
NC	14.30 ± 1.25	11.17 ± 0.73	7.85 ± 0.05	23 ± 0.30	1536 ± 89

$\Delta p/m_c^2$  strongly decreases with the diameter from 0.6 to 0.8 mm, and it is attenuated for larger diameters. This trend is due to the large coolant gasification obtained with small diameters. Rearranging the simplified Darcy's equation for hydraulic systems, one can obtain:

$$\frac{\Delta p}{m_c^2} = \frac{\xi}{\bar{\rho}} \quad (10)$$

where  $\xi$  is the total hydraulic resistance, which depends on the pipe length, cross-sectional area or concentrated losses like sudden contractions or expansions, and geometrical corners, and  $\bar{\rho}$  is the average coolant density. Strong restrictions of the orifice diameter lead to an increase in hydraulic resistance and a large drop in density, which explains the trend observed in Fig. 12f.

Finally, Fig. 12g displays the pressure drop achieved along the channels with the mass flow rate. The pressure jump increases with the

mass flow rate by a power equal to 0.84. Note that the exponent is lower than 2 displayed in Eq.(10) because the density is function of the mass flow rate due to the upstream cavitation.

### 3.2. Nozzle erosion Suppression and thermal management

The effectiveness of introducing a regenerative cooling system working with liquid nitrous oxide for the thermal control of the heat fluxes developed in the nozzle is discussed. The idea of regenerative cooling was raised after performing previous experimental campaigns in which nozzle erosion was observed in 44 tests for many motor configurations and operative conditions comparable to those considered in this work [17]. Most of these tests exhibited nozzle erosion, depending on the operative burning time and mass flow rate. To mitigate this issue, we first developed a regenerative cooling system based on cryogenic oxygen in our previous work, and we successfully demonstrated the capability of the system to suppress nozzle erosion in any condition [19]. Because of the many benefits introduced by nitrous oxide for in-space propulsion applications, we investigate the cooling capability of LN<sub>2</sub>O in comparison with LOX in this paper.

The occurrence of nozzle erosion is not obvious with the LN<sub>2</sub>O/HDPE couple because the flame temperature is typically lower than LOX/HDPE and the mixture is less rich in oxidizing species and diluted by nitrogen. For this reason, an additional firing test named Test NC (No Cooling) was performed in order to highlight the persistent need for a

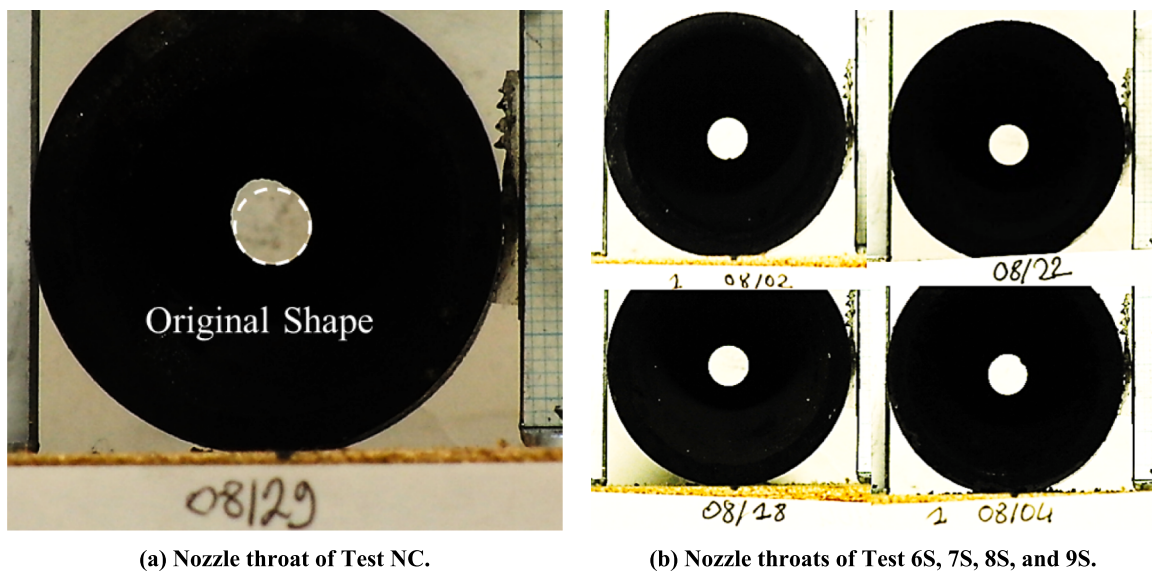


Fig. 13. Comparison of the nozzle throats of tests performed with and without a cooling system.

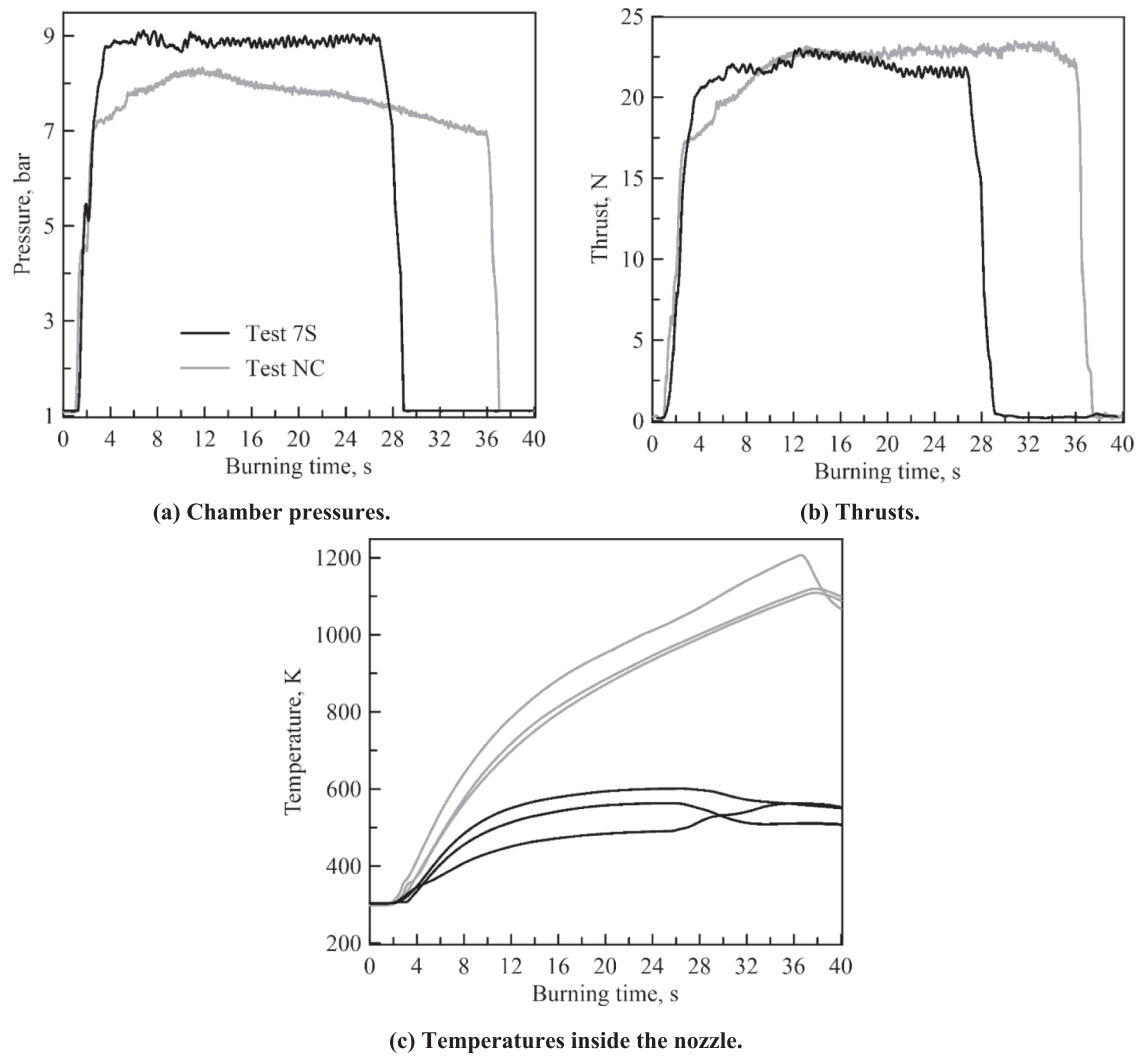
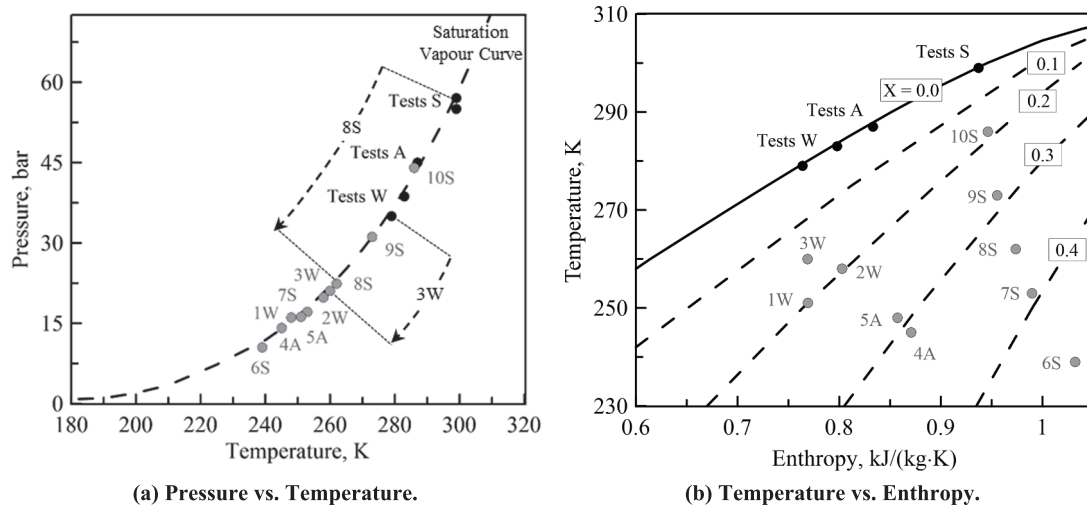


Fig. 14. Comparison of Test NC and Test 7S.



**Fig. 15.** Representation of the coolant pressure and temperature upstream (black dots) and downstream (grey dots) of the cavitation orifice.

**Table 5**

Coolant density, vapour quality, and void fraction downstream of the cavitation orifice.

Test	Density, $\rho_2$ , kg/m <sup>3</sup>	Void fraction, $\alpha_2$	Vapour quality, $X_2$
1 W	186.08	0.852	0.201
2 W	214.19	0.826	0.197
3 W	278.02	0.758	0.153
4A	109.55	0.927	0.312
5A	132.44	0.907	0.290
6S	59.04	0.969	0.458
7S	107.75	0.935	0.392
8S	152.64	0.897	0.349
9S	242.54	0.808	0.283
10S	410.78	0.598	0.183

cooling system with LN<sub>2</sub>O and the benefits of using regenerative cooling. The operative conditions of Test NC, which are similar to Test 7S, are summed up in [Table 4](#).

[Fig. 13](#) represents the comparison of the nozzle throat pictures of Test 6S, 7S, 8S, and 9S with Test NC. These tests are just an example, and the same comments are valid for Tests A and W. Test NC exhibited localized nozzle erosion with an average diameter enlargement of 6 to 6.69 mm. In contrast, the throats of tests using regenerative cooling

remained unaltered, and the structural integrity of the graphite was conserved. Indeed, the measured throat diameters are 6.02, 6.02, 6.01, and 6.01 mm, respectively. No cracking was observed from a superficial inspection of the inner and outer graphite surfaces. The nozzles have been reused several times, demonstrating their reliability for multiple ignitions, a crucial feature for space missions.

[Fig. 14](#) compares the chamber pressures, the temperatures measured inside the nozzle, and the thrusts of the Test NC and 7S, which have been carried out with similar oxidizer mass flow rates. Differently from Test 7S, the chamber pressure of Test NC decreases from 8 to around 7 bar due to the throat enlargement. Observing the thrust signals, both Test NC and Test 7S reach a steady thrust value around 23 N close, which remains constant during the burning time.

The nozzle temperatures continuously increase in Test NC, reaching 1200, 1119, and 1108 K at 3, 5, and 8.5 mm from the throat inner surface. On the other hand, the temperatures of Test 7S are limited to 600, 562, and 490 K by the cooling system, and they are independent of the burning time. These results give evidence of the need for implementing such technologies in real in-space applications with burning times higher than 30 s; indeed, even accepting nozzle erosion, the temperatures recorded in Test NC are intolerable for the spacecraft structures and bus.

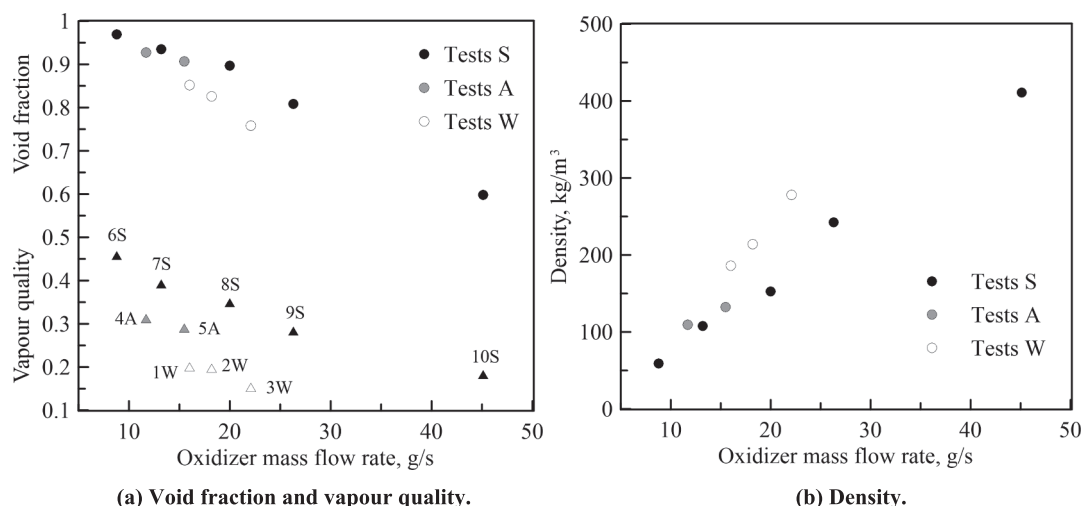


**Fig. 16.** Coolant multiphase properties downstream of the cavitation orifice.

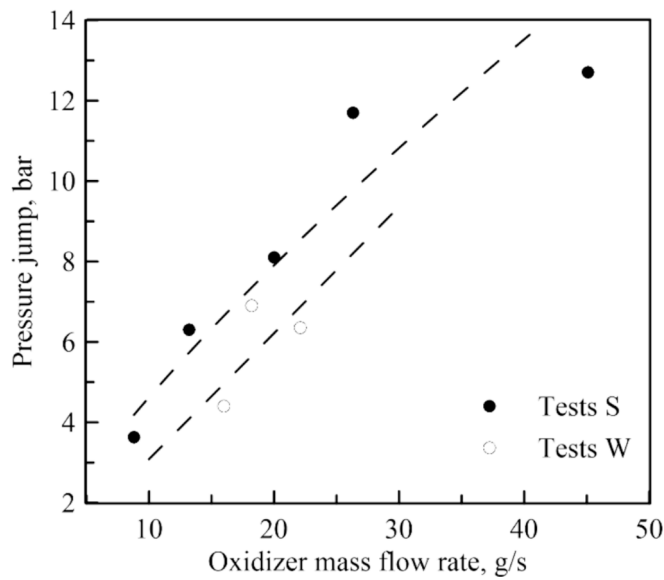


Fig. 17. Representation of pressure jump along the cooling channels vs mass flow rate.

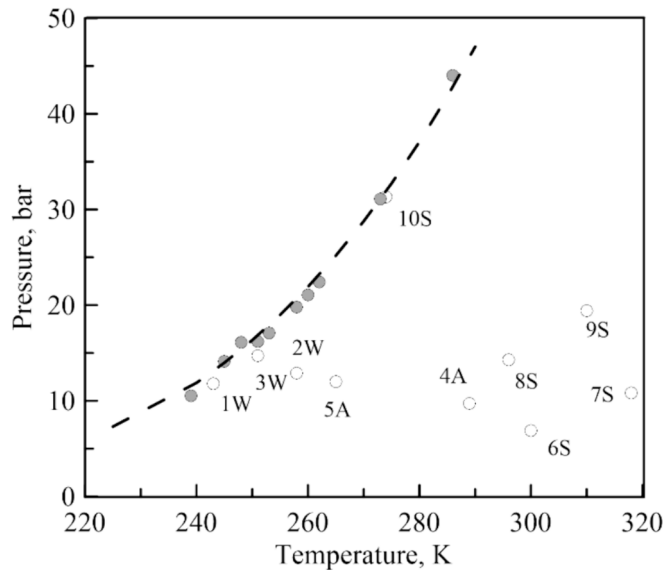


Fig. 18. Representation of the coolant state upstream (grey dots) and downstream (white dots) of the cooling system.

### 3.3. Analysis of coolant state at the recorded stations

#### 3.3.1. Cavitation orifice

The largest changes in coolant pressure and temperature have been recorded through the cavitation orifice and the cooling channels. Therefore, the coolant phase state is evaluated and discussed upstream and downstream of the cavitation orifice and the cooling system. Starting from the cavitation orifice, Fig. 15a shows that the coolant  $p-T$  state downstream of the orifice follows the saturation vapour curve in all the tests. Assuming that the coolant phase is completely liquid at the orifice inlet ( $X_1 = \alpha_1 = 0$ ), the vapour fraction could be evaluated using Eq. (2). The calculated coolant density, void fraction, and vapour quality downstream of the orifice are summed up in Table 5. The amount of gas developed by cavitation can be graphically evaluated by the  $T-s$  graph displayed in Fig. 15b. In subsection 3.1, we compared Test 3 W and Test 8S with the same mass flow rate of around 20 g/s. Fig. 15b clearly

displays that the gas fraction of Test 8S is higher than Test 3 W; therefore, the same mass flow rate is obtained with different tank pressures regulating the gas fraction by the orifice diameter. Consequently, Test 8S shows a larger temperature and pressure drop than Test 3 W, which is clearly highlighted by the arrows in Fig. 15a. The effect of the gas fraction on the cooling performance is discussed in the next sections.

Fig. 16 displays the mentioned multiphase quantities of Tests W, A, and S versus the coolant mass flow rate. As a general trend, the vapour quality and void fraction decrease with the flow rate, and in turn the density displays the opposite trend. The ambient temperature (or pressure tank) affects the coolant gasification. For instance, let us focus on Test 1 W and 5A, showing the same mass flow rate of around 16 g/s at different ambient temperatures of 279 and 287 K, respectively. The former develops a vapour quality and density equal to 0.201 and 186 kg/m<sup>3</sup>, while the latter equal to 0.290 and 132 kg/m<sup>3</sup>. In conclusion, with the aim of targeting a specific amount of mass flow rate, the inlet vapour quality of the cooling channels increases with the ambient temperature. Consequently, as displayed in Fig. 17, the pressure jump through cooling channels of Tests S is higher than Tests W because of the lower coolant density.

#### 3.3.2. Cooling system

Now, let us focus on the coolant pressure and temperature jumps through cooling channels. Fig. 18 displays the coolant upstream and downstream p-T conditions of the cooling system, compared with the saturation vapour curve. It can be noticed that the outlet conditions of some tests still fall close to the vapour curve, exhibiting a negative temperature jump; on the other hand, others deviate from the saturation line with a positive temperature jump. The sign of the temperature jump is related to the void fraction, or the mixture density, at the inlet of the cooling channels developed through the cavitation orifice. When the fluid phase is close to the liquid state, the gasification through cooling channels involves a strong expansion, leading to the fluid cooling even though it is heated by the hot nozzle. In other words, the fluid transformation through the cooling channels is similar to that observed through the cavitation orifice. Indeed, tests with a higher inlet density, such as Tests W, 5A, and 10 S, exhibit a negative temperature jump, while the remaining Tests S and Test 4A display a positive temperature difference.

In this case, the evaluation of the exit gas fraction,  $X_3$ , is complicated by the fact that the vaporization is simultaneously triggered by the coolant heating and the pressure drop. Therefore, an additional assumption is required for the evaluation of the final gas fraction. As mentioned above, half of the tests follow the saturation curve, while others deviate, showing a temperature rise. For this reason, a rough estimation can be obtained by assuming that the vaporization is mainly promoted by the pressure drop following the saturation curve, and then the resulting multiphase mixture is heated at constant pressure. Observing Fig. 19 and considering Test 9S as an example, the vaporization occurs from state 2 to intermediate state 2i, and the multiphase mixture is isobarically heated from the state 2i to 3 (with  $X_3 = X_{2i}$ ). Consequently, Eq. (2) can be arranged as jump equation between the state 2 and the intermediate one, 2i:

$$(1 - X_2)hs_{l,2} + X_2hs_{v,2} + \frac{G^2}{\rho_2^2 2} = (1 - X_{2i})hs_{l,2i} + X_{2i}hs_{v,2i} + \frac{G^2}{\rho_{2i}^2 2} \quad (11)$$

Then, the coolant multiphase properties at state 3 can be evaluated by Eq. (3). The calculated coolant density, void fraction, and vapour quality downstream of the channels (state 3) are summed up in Table 6.

Fig. 20a displays the vapour quality jump achieved by the passage of the coolant in the channels. The higher the gas fraction in the inlet, the higher the vapour quality jump. Tests S still developed the largest amount of steam among all the other tests. Fig. 20b displays that the temperature jump through the cooling system increases with the average vapour quality,  $(X_2 + X_3)/2$ . A positive trend in the temperature

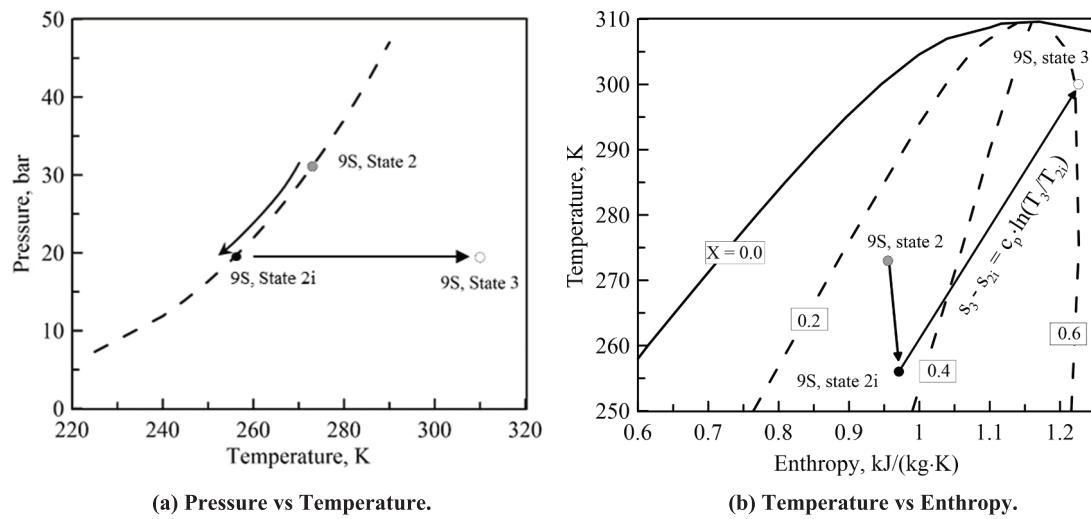


Fig. 19. Schematization of the vaporization and heating process through cooling channels.

**Table 6**

Coolant density, vapour quality, and void fraction downstream of the cooling system.

Test	Density, $\rho_3$ , kg/m <sup>3</sup>	Void fraction, $\alpha_3$	Vapour quality, $X_3$
1 W	122.59	0.910	0.228
2 W	114.48	0.920	0.273
3 W	173.63	0.863	0.189
4A	68.37	0.959	0.354
5A	89.20	0.943	0.330
6S	36.14	0.983	0.480
7S	59.91	0.967	0.444
8S	87.21	0.950	0.407
9S	128.07	0.918	0.366
10S	278.74	0.764	0.233

jump with the coolant gasification is observed. These results further confirm that the tests characterized by a positive temperature jump coincide with the most gasified ones.

### 3.3.3. Gas heat transfer coefficient and coolant heat transfer coefficient

The computed temperatures and heat transfer coefficients at the hot and cold sides evaluated by the methodology illustrated in subsection 2.1.1 are here discussed and summarized in Table 7.

The heat transfer coefficient at the hot side evaluated by Eq.(5) is displayed in Fig. 21. Because the throat area is constant among the tests, the gas heat transfer coefficient,  $h_g$ , is mainly correlated to the total mass flow rate.  $h_g$  increases from 636 to 3694 W/(m<sup>2</sup>•K) by increasing  $\dot{m}_{tot}$  from around 10 to 50 g/s. The experimental correlation is given by

$$h_g = 143.09 \dot{m}_{tot}^{0.887} \quad (12)$$

As shown,  $h_g$  increases with  $\dot{m}_{tot}$  with the power of 0.887 close to 0.80 of Bartz's power law from around 500 to 3500 W/(m<sup>2</sup>•K), but it is in average the 20 % of that calculated by the theoretical formula [33].

Fig. 22 displays the coolant heat transfer coefficient,  $h_c$ , with the mass flow rate per unit of channel.  $h_c$  increases from 3912 to 21181 W/(m<sup>2</sup>•K) by increasing the flow rate per channel from around 3 to 15 g/s. A clear trendline of  $h_c$  with  $\dot{m}_c$  is recognized, considering all the tests except Test 6S, 8S and 9S, whose heat transfer coefficients are on average lower than the other tests performed at the same mass flow rate. The cooling

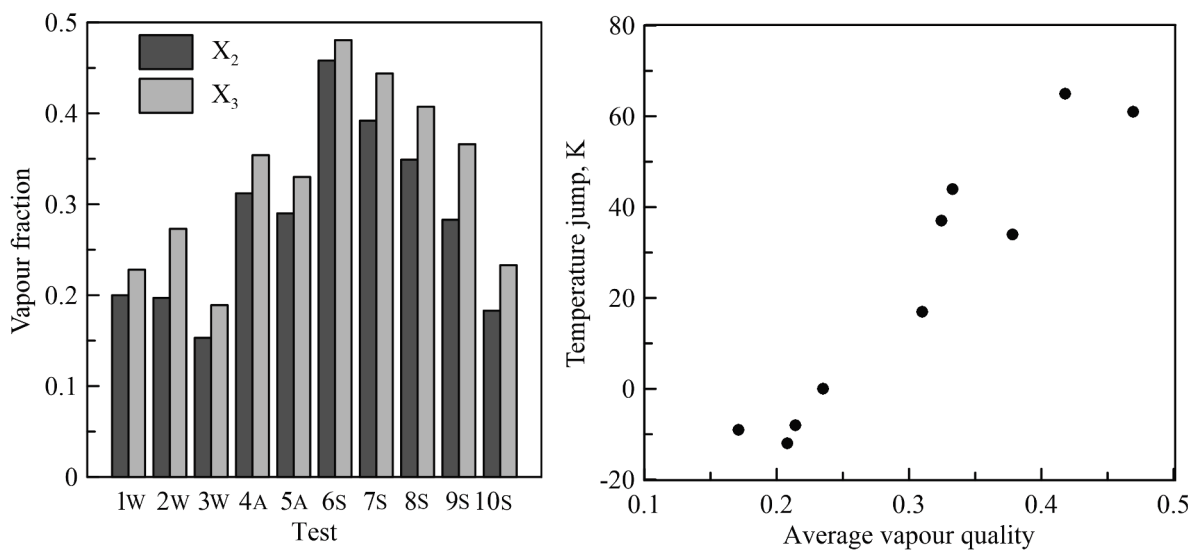
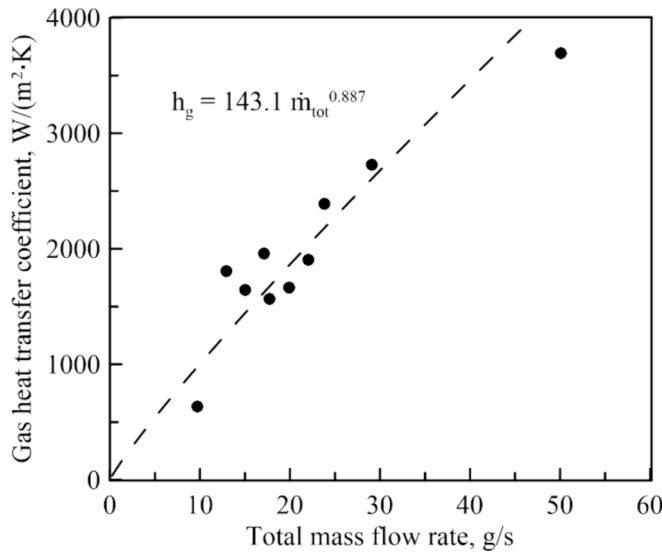
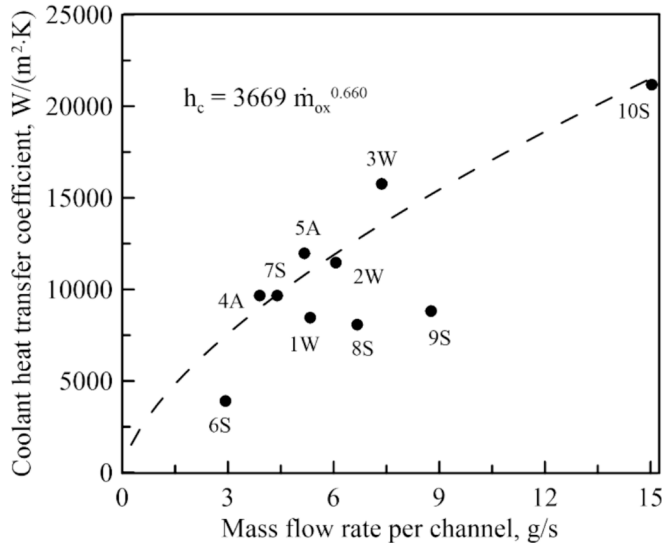


Fig. 20. Representation of the vapour quality and temperature jump through cooling channels.

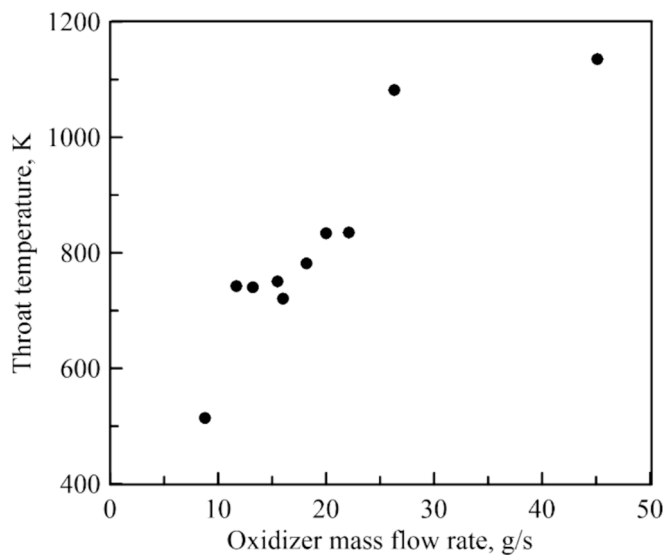
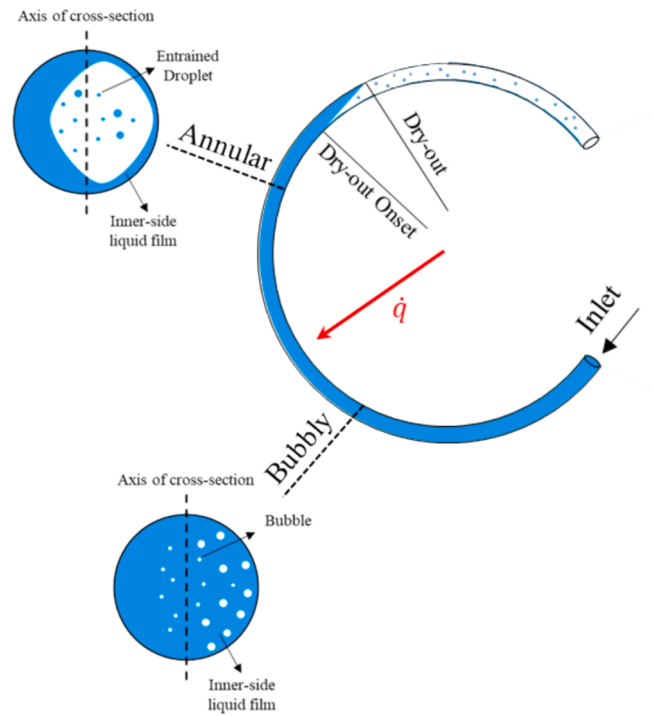
**Table 7**

Calculated density, void fraction, vapour quality and mixture properties.

Test	Hot Temperature, K	Cold Temperature, K	Gas Heat Coefficient, W/(m <sup>2</sup> •K)	Coolant Heat Coefficient, W/(m <sup>2</sup> •K)
1 W	721 ± 6	402 ± 5	1566 ± 59	8455 ± 320
2 W	782 ± 7	374 ± 4	1666 ± 56	11472 ± 383
3 W	835 ± 8	376 ± 5	2390 ± 70	15754 ± 462
4A	742 ± 7	404 ± 4	1807 ± 73	9669 ± 393
5A	750 ± 7	508 ± 4	1959 ± 74	11976 ± 453
6S	514 ± 5	416 ± 4	636 ± 87	3912 ± 533
7S	740 ± 7	425 ± 5	1645 ± 74	9665 ± 432
8S	834 ± 7	464 ± 5	1905 ± 71	8075 ± 301
9S	1082 ± 8	509 ± 5	2729 ± 65	8812 ± 209
10S	1140 ± 8	401 ± 5	3694 ± 65	21181 ± 374

**Fig. 21.** Hot gas heat transfer coefficient vs the total mass flow rate.**Fig. 22.** Coolant heat transfer coefficient vs mass flow rate per channel (trendline obtained excluding Test 6S, 8S, and 9S).

performance of these out-of-trend tests could be compromised by the large amount of steam developed along the cooling channels. Indeed, these tests belong to the group, featuring the highest level of vapour

**Fig. 23.** Nozzle temperature at the throat vs oxidizer mass flow rate.**Fig. 24.** Sketch of the LOX flow field inside the helical channel.

quality and positive temperature jump, as displayed in Fig. 18 and Fig. 20a. For all the other tests,  $h_c$  increases with  $\dot{m}_c$  per channel following the power law:

$$h_c = 3669 \dot{m}_c^{0.660} \quad (13)$$

Note that the exponent of  $\dot{m}_c$  in Eq. (13) lower than that displayed in Eq. (12) is in agreement with the throat temperatures displayed in Fig. 23.

The throat temperatures increase with the flow rate because the cooling performance increases by the exponent 0.66, which is lower than that of the heat transfer coefficient on the hot side of 0.887. This growth is particularly detrimental for Tests S, which achieved higher throat temperatures under the same mass flow rate conditions. For instance, Test 9S showed a throat temperature of 1082 K with a mass

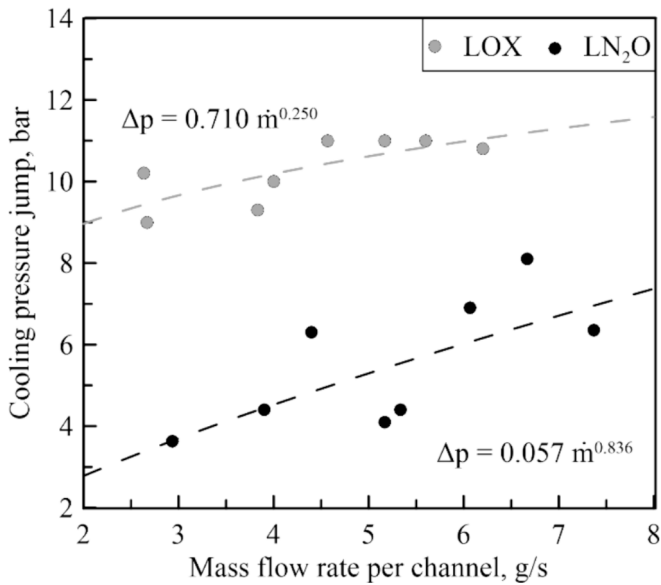


Fig. 25. Comparison of jump pressure vs oxidizer mass flow rate per channel between LOX and LN<sub>2</sub>O.

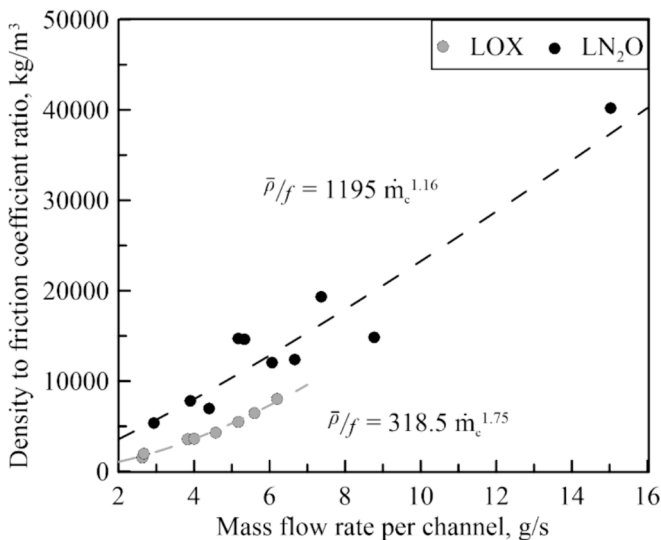


Fig. 26. Representation of  $\bar{\rho}/f$  at different operating conditions with LOX and LN<sub>2</sub>O.

flow rate of 26 g/s, while Test 3 W a temperature of 835 K with 22 g/s. The highest throat temperature of around 1200 K is observed in Test 10S with  $\dot{m}_c$  at 45 g/s. Note that the motor was designed for a maximum mass flow rate of 30 g/s, and the cooling system is still effective in this out-of-design test.

### 3.4. Comparison with cryogenic oxygen

In this section, the cooling performance of liquid nitrous oxide is compared with that of cryogenic oxygen [19]. From an operative point of view, nitrous oxide introduces two main benefits: it is storable at room temperature, hence no precautions are required for the tank thermal insulation and valves, and it can be used in a self-pressurized fashion, dismissing additional pressurization systems. These characteristics greatly simplified the running of experimental firing tests. The multiphase flow field of LOX and LN<sub>2</sub>O is the first main difference between the two oxidizers. As shown in Fig. 24, because LOX is pushed

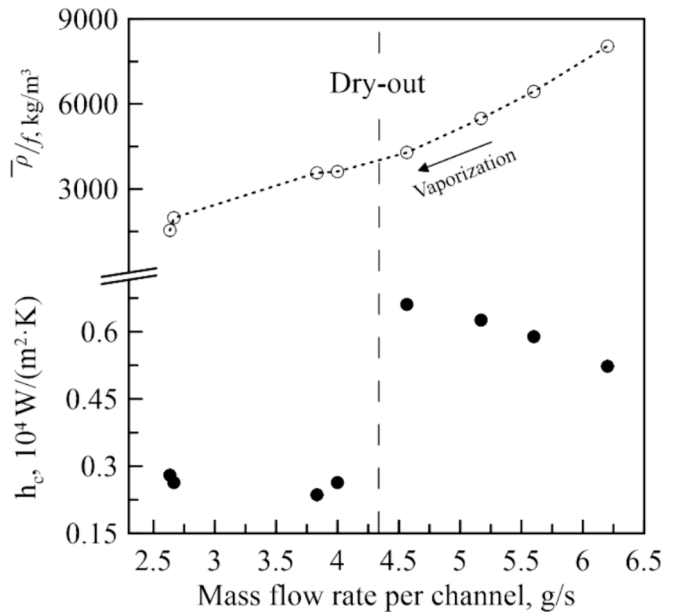


Fig. 27. Coolant heat transfer coefficient and  $\bar{\rho}/f$  vs coolant mass flow rate with LOX [19].

inside the channel in liquid phase, the multiphase flow evolves from bubbly to annular. The dry-out could occur in the case of large coolant vaporization. On the other hand, LN<sub>2</sub>O is injected with a void fraction higher than 0.5 in any test (see Fig. 16a); therefore, the bubbly regime is skipped and the coolant is supplied as annular flow.

The cooling performance is compared here in terms of pressure jump and nozzle temperatures. Fig. 25 represents a weak sensitivity of  $\Delta p$  from  $\dot{m}_c$  with a power of 0.25 using LOX. The  $\Delta p$  was approximately constant around 10 bar by varying the flow rate per channel from 2.5 to 6.0 g/s. In the case of liquid nitrous oxide, the  $\Delta p$  increases with  $\dot{m}_c^{0.836}$  in a range of 2.5 to 15 g/s. Considering the same range of  $\dot{m}_c$  for both the oxidizers, the pressure jump of LOX is higher than that observed with LN<sub>2</sub>O.

These trends can be easily discussed with the support of the Darcy–Weisbach equation:

$$\frac{\bar{\rho}}{f} = \frac{\dot{m}_{ox}^2}{2(p_2 - p_3)} \frac{L_{ch}}{A_{ch}^2 D_h} \quad (14)$$

where the channel area,  $A_{ch}$ , the hydraulic diameter,  $D_h$ , and the channel length,  $L_{ch}$ , are equal to  $10^{-6} \text{ m}^2$ ,  $10^{-3} \text{ m}$  and  $0.452 \text{ m}$ , respectively. The left on side of Eq. (14) evaluated with both oxidizers is displayed in Fig. 26. Assuming a constant friction coefficient, the average density of LOX was lower than that of LN<sub>2</sub>O, suggesting that the former gasified much more than the latter. This result was expected because the temperature of the nozzle external surface is extremely higher than the typical vaporization temperatures of cryogenic oxygen (equal to around 154 K at the critical point).

The fluid density (or gas fraction) is strongly related to the mass flow rate in the case of LOX with a power equal to 1.75 compared with LN<sub>2</sub>O of 1.16. For this reason, LOX exhibited a weaker dependence of the pressure jump on the flow rate.

Regarding the coolant heat transfer coefficient, Fig. 27 displays the trend of  $h_c$  with the mass flow rate per channel in the case of LOX. It can be observed that  $h_c$  decreased with the mass flow rates higher than 4.5 g/s, and it was enhanced by decreasing  $\bar{\rho}/f$ ; on the other hand, it was approximately constant around 2500 W/(m<sup>2</sup>·K) for lower flow rate values. This counter-intuitive trend was extensively explained in our previous work.

The  $h_c$  primarily depends on the Reynolds number, which in turn is

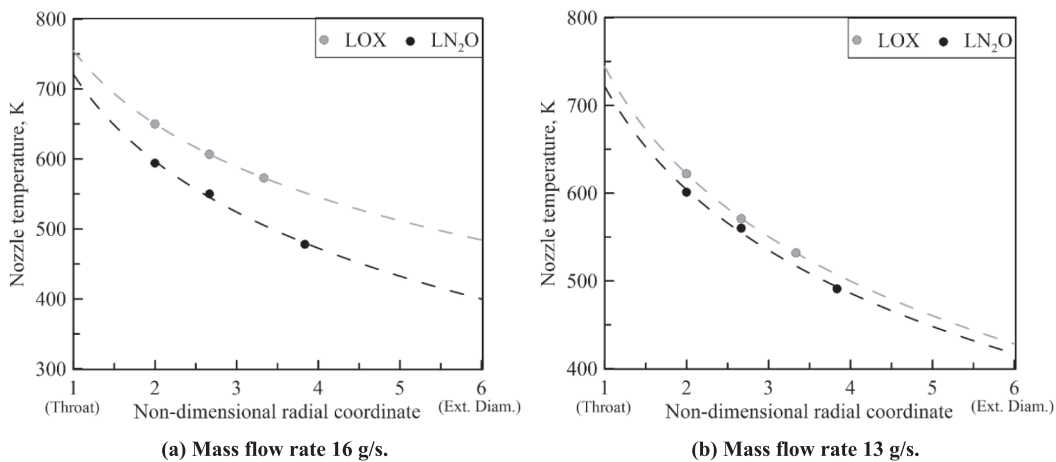


**Fig. 28.** Comparison of the nozzle temperatures between LOX and LN<sub>2</sub>O at two different mass flow rates.

**Table 8**

Summary of benefits and drawbacks of using regenerative cooling based on LN<sub>2</sub>O and LOX.

Benefits LOX and LN <sub>2</sub> O	Drawbacks LOX	Drawbacks LN <sub>2</sub> O
<ul style="list-style-type: none"> <li>Suppression of nozzle erosion and improvement of motor performance in terms of thrust and specific impulse.</li> <li>Greater reusability with the capability of multiple ignitions at the same performance.</li> <li>Self-handling of the chamber heat fluxes and elimination of heavy TPS for the thermal insulation of the satellite from the nozzle.</li> </ul>	<ul style="list-style-type: none"> <li>Higher complexity of the overall propulsion system due to the introduction of additional pipes and helical printed channels.</li> <li>Lower repeatability and control in the test conditions because of the thermal coupling of the feeding line with the combustion chamber.</li> </ul>	<ul style="list-style-type: none"> <li>Higher complexity of the overall propulsion system due to the introduction of additional pipes and helical printed channels.</li> </ul>

related to the mass flow rate and the flow viscosity. The viscosity is dependent on the vaporization degree of the coolant. Because the vaporization decreases with  $\dot{m}_c$  (see Fig. 27), the flow rate plays two

contrasting roles in the Reynolds number [34,35,36]. If the effect of the viscosity drop due to the vaporization is dominating on the Reynolds number, large  $\dot{m}_c$  could negatively affect  $h_c$ . However, the enhancement due to the vaporization was limited for low  $\dot{m}_c$  by the dry-out.

The trend displayed by cryogenic oxygen differs from that exhibited by nitrous oxide in Fig. 22. A positive trend of  $h_c$  with  $\dot{m}_c$  is displayed with LN<sub>2</sub>O. Differently from cryogenic oxygen, most coolant gasification occurs through the orifice upstream of the cooling system. Because the void fraction at the inlet of the cooling system is higher than 0.5 in all the tests except Test 10 (see Table 5), the fluid viscosity is close to the vapour state for any mass flow rate. For this reason, the Reynolds number is positively dependent on the flow rate. In analogy with cryogenic oxygen, tests featuring high gas fractions, such as Tests S, exhibit lower cooling performance.

In a wider framework, the cooling performance of LOX is lower than that of LN<sub>2</sub>O at any operating condition. The highest value of  $h_c$  of 7 kW/(m<sup>2</sup>•K) with LOX is observed at 4.5 g/s; at the same mass flow rate per channel, LN<sub>2</sub>O exhibited a cooling coefficient of 10 kW/(m<sup>2</sup>•K). This feature is typical of cooling systems working with cryogenic coolants. Although the thermodynamic and transport properties of the oxidizers are mostly the same, LOX flow is characterized by large thermal gradients between the channel surface and the coolant core, leading to a detrimental reduction of the thermal transport properties [37,38].

The higher cooling performance of liquid nitrous oxide is further

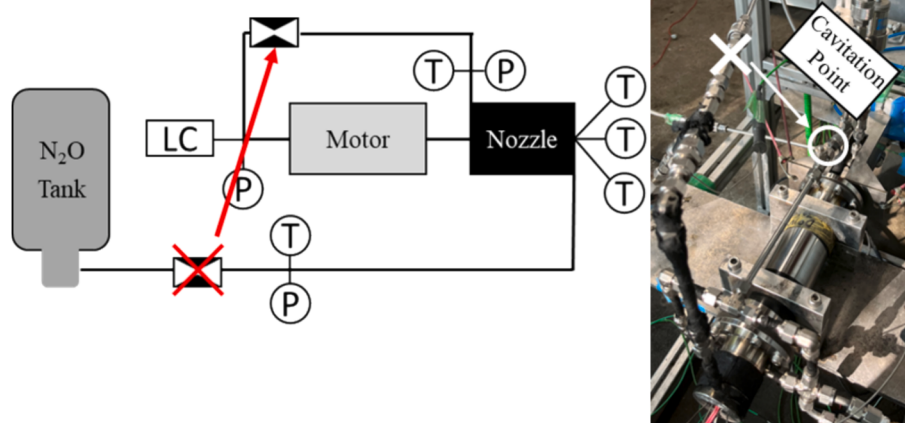


**Fig. 29.** Representation of the alternative position of the cavitation point in the propulsion system.

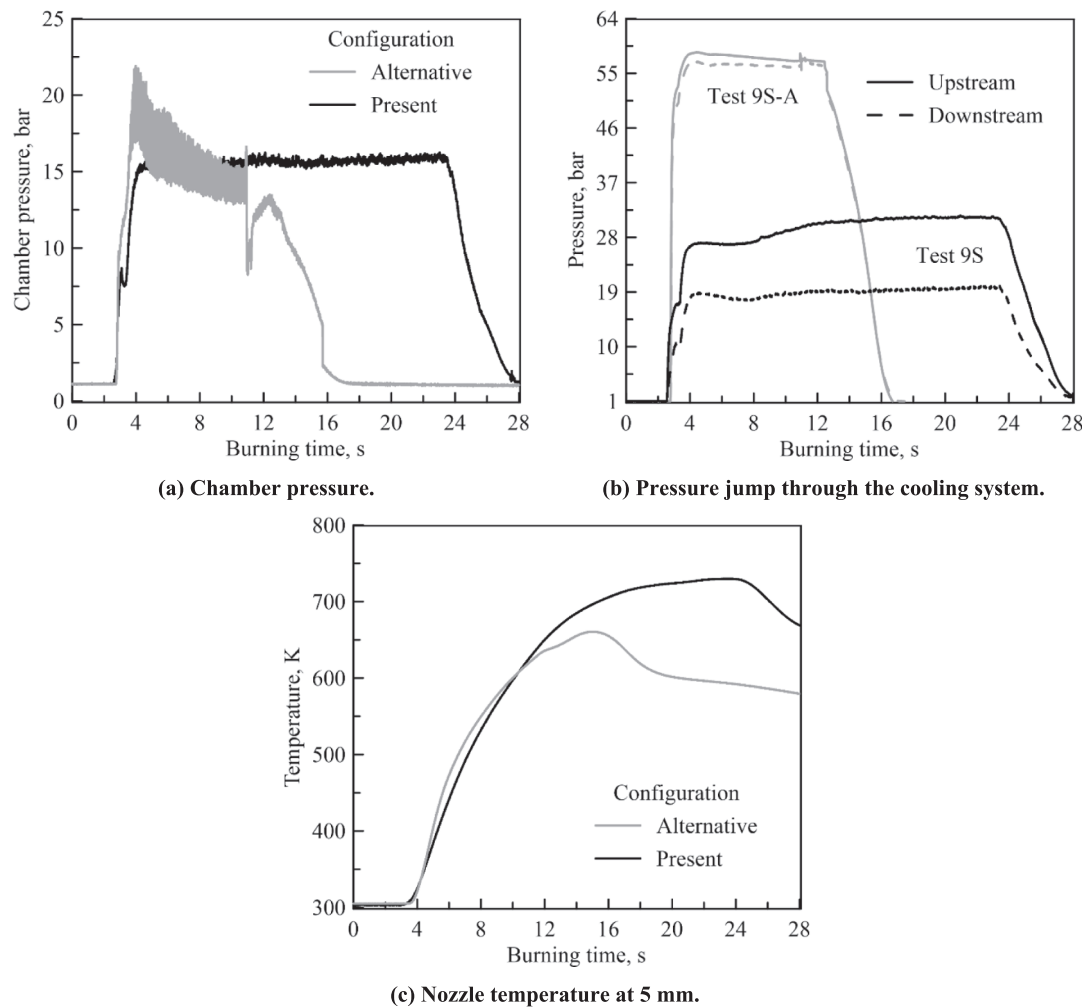


**Fig. 30.** Comparison of the proposed and the alternative experimental configuration.

highlighted by Fig. 28, which displays a comparison of nozzle temperatures with LOX at two different mass flow rates, 16 g/s and 13 g/s. Nozzle temperatures were lower using nitrous oxide in the former case at 16 g/s. The latter comparison at 13 g/s is particular because it coincides with the best performance of LOX and the worst performance of LN<sub>2</sub>O. Even then, nitrous oxide demonstrated higher cooling capabilities than oxygen.

Finally, the benefits and drawbacks of using regenerative cooling with cryogenic oxygen claimed in Ref.[19] are summed up in Table 8. The use of liquid nitrous oxide still enjoys all the mentioned benefits. In addition, because the pressure drop and the heat transfer are marginally affected by the vaporization, which is controlled by the cavitation orifice, the reliability and the repeatability of the firing tests have been largely improved with LN<sub>2</sub>O.

### 3.5. Influence of the cavitation point location

The cavitation orifice is an essential element for our experimental setup, because it is the controlling device of the oxidizer mass flow rate. As above mentioned, the amount of steam developed by cavitation and flowing inside cooling channels is primarily related to the orifice diameter. An alternative configuration is investigated, where the orifice is moved downstream of the cooling system few millimeters upstream of the combustion chamber (see Fig. 29). In contrast with the previous configuration, the coolant is completely liquid at the inlet of the cooling system.

However, the results are actually counter-intuitive. In order to

compare the two configurations, an additional test was carried out with the same mass flow rate as Test 9S, and, for this reason, it is here labelled as Test 9S-A. The results have been compared in Fig. 30. Fig. 30a represents the comparison of the chamber pressure, displaying the establishment of combustion instability in Test 9S-A with oscillation amplitudes of 3 bar. Because of the instability, the test was shut off after just 10 s, which was the time required by the system to reach the average operative pressure of 14 bar. Fig. 30b displays the comparison of the pressure jumps between the two tests. The measured  $\Delta p$  was around 2 bar in Test 9S-A, 6 times lower than Test 9S. The reason relies on the higher coolant density achieved with the alternative configuration than the previous one. The coolant vaporization through cooling channels was poor, and most of the gasification occurs downstream by the cavitation orifice. Finally, Fig. 30c represents the comparison of the temperatures measured at 5 mm from the throat surface. Although no steady state was achieved in the alternative configuration, the signals are mostly overlapped during the heating time, suggesting no relevant thermal benefits. Although further research is required about this issue, we can deduce that the product of  $h_c$  and  $(T_{wc} - T_c)$  in Eq. (6) is constant among the two tests. Because Test 9S develops a low  $T_c$  downstream of cavitation orifice, we can deduce that  $h_c$  is higher in Test 9S-A. Moreover, the coolants phase of Test 9S-A in the channels is close to the liquid phase, while a multiphase mixture is present in Test 9S. In conclusion, we can deduce from this study that, in the current setup, the best location for coolants cavitation is upstream of cooling channels.

#### 4. Conclusions

The results of an experimental campaign for the investigation of a regenerative cooling system in hybrid rocket engines based on saturated liquid nitrous oxide are presented in this paper. The novelty of the work consists in the use of a cooling system based on saturated liquid nitrous oxide, wrapping the external surface of a COTS graphite nozzle. The harsh heat fluxes developed in the nozzle have been successfully handled by the active cooling system. The aim of the work is to demonstrate and investigate the cooling capability of liquid nitrous oxide. Ten firing tests have been performed at different operating conditions in order to investigate the reliability of the concept at different mass flow rates. The mass flow rate was controlled by cavitation, and it ranged between 9 and 45 g/s, with a thrust range including between 15 and 100 N. The nozzle temperatures are measured at 3, 5, and 8.5 mm from the throat inner surface. The coolant pressure and temperature are measured upstream and downstream of the cavitation orifice and cooling system, respectively. The coolant heat transfer coefficient and gas fraction are indirectly evaluated based on the measured experimental data. Nozzle erosion was successfully suppressed in all the tests, even in the out-of-scale one performed with a mass flow rate of 45 g/s. The most relevant observations are summarized below:

- The highest pressure jump along the pressure chain was observed through the cavitation orifice placed upstream of the cooling system, depending on the required mass flow rate and orifice diameter. Test 8S and Test 10S, performed at 9 and 45 g/s, display the largest and the smallest pressure drop of 47.37 and 18.91 bar at the cavitation orifice, respectively; on the other hand, the former shows a pressure drop at the cooling channels of 4.39 bar, the latter of 12.77 bar.
- The outlet coolant temperature is far from the activation temperature of nitrous oxide decomposition. The highest temperature is recorded for Test 7S, performed with a mass flow rate of 13.2 g/s.
- The coolant and hot gas heat transfer coefficients directly increase with the mass flow rate, with a power of 0.66 and 0.887, respectively. The highest values are observed in Test 10 S, which are 3694 and 21,181 W/(m<sup>2</sup>·K), respectively.
- The nozzle temperatures increase with the mass flow rates, leading to a maximum throat temperature of 1200 K in the Test 10S.
- Liquid nitrous oxide shows higher cooling performance compared with cryogenic oxygen. Liquid nitrous oxide gains all the benefits of LOX, with the additional advantage of increasing the predictability of motor performance in any aspect.
- The influence of the position of the cavitation orifice on the motor performance was investigated, introducing an alternative configuration in which the orifice is placed downstream of the cooling system. The results of the alternative configuration show no improvements in cooling performance and promotion of combustion instability.

#### Declaration of competing interest

The authors declare that they have no known competing financial interests or personal relationships that could have appeared to influence the work reported in this paper.

#### Data availability

Data will be made available on request.

#### Acknowledgement

This research was supported by the Japan Society for the Promotion of Science (JSPS).

#### References

- [1] T. Shimada, C. Carmicino, A. Karabeyoglu, Hybrid rocket (volume II), Aerospace 9 (2022) 233, <https://doi.org/10.3390/aerospace9050233>.
- [2] C. Carmicino, Advances in hybrid rocket technology and related analysis methodologies, Aerospace 6 (2019) 128, <https://doi.org/10.3390/aerospace6120128>.
- [3] A. Okninski, W. Kopacz, D. Kaniewski, K. Sobczak, Hybrid rocket propulsion technology for space transportation revisited - propellant solutions and challenges, FirePhysChem 1 (2021) 260–271, <https://doi.org/10.1016/j.fpc.2021.11.015>.
- [4] F. Barato, Review of alternative sustainable fuels for hybrid rocket propulsion, Aerospace 10 (2023) 643, <https://doi.org/10.3390/aerospace10070643>.
- [5] C. Paravan, A. Hashish, V. Santolini, Test Activities on Hybrid Rocket Engines: Combustion Analyses and Green Storable Oxidizers—A Short Review, 10 (2023) 572, [Doi: 10.3390/aerospace10070572](https://doi.org/10.3390/aerospace10070572).
- [6] H. Tian, L. He, R. Yu, S. Zhao, P. Wang, G. Cai, Y. Zhang, Transient investigation of nozzle erosion in a long-time working hybrid rocket motor, Aerosp. Sci. Technol. 118 (2021) 106978, <https://doi.org/10.1016/j.ast.2021.106978>.
- [7] D. Altman, A. Holzman, Overview and History of Hybrid Rocket Propulsion. Fundamentals of Hybrid Rocket Combustion and Propulsion, edited by K. Kuo, M. Chiaverini, AIAA Progress in Astronautics and Aeronautics, 218 (2007) 1–36.
- [8] K. Kuo, M. Chiaverini, Challenges of Hybrid Rocket Propulsion in the 21st Century, Fundamentals of Hybrid Rocket Propulsion, edited by M. Chiaverini, and K. Kuo, AIAA Progress in Astronautics and Aeronautics, 218 (2006) 593–638, [Doi: 10.2514/5.9781600866876\\_0593.0638](https://doi.org/10.2514/5.9781600866876_0593.0638).
- [9] R. Acharya, K. Kuo, Effect of pressure and propellant composition on graphite rocket nozzle erosion rate, J. Propuls. Power 23 (2007) 1242–1254, <https://doi.org/10.2514/1.24011>.
- [10] L. Kamps, Y. Saito, R. Kawabata, M. Wakita, T. Totani, Y. Takahashi, H. Nagata, Method for determining nozzle-throat-erosion-history in hybrid rockets, J. Propuls. Power 33 (2017) 1369–1377, <https://doi.org/10.2514/1.B36390>.
- [11] T.D. Swanson, G.C. Birur, NASA thermal control technologies for robotic spacecraft, Appl. Therm. Eng. 23 (2003) 1055–1065, [https://doi.org/10.1016/S1359-4311\(03\)00036-X](https://doi.org/10.1016/S1359-4311(03)00036-X).
- [12] O. Uyanna, H. Najafi, Thermal protection systems for space vehicles: a review on technology development, current challenges and future prospects, Acta Astronaut. 176 (2020) 341–356, <https://doi.org/10.1016/j.actaastro.2020.06.047>.
- [13] C. Glaser, J. Hijkema, J. Anthoine, Bridging the technology gap: strategies for hybrid rocket engines, Aerospace 10 (2023) 901, <https://doi.org/10.3390/aerospace10100901>.
- [14] H.G. Price, Cooling of high-pressure rocket thrust chambers with liquid oxygen, J. Spacecr. Rockets 18 (4) (1980) 338–343, <https://doi.org/10.2514/3.57826>.
- [15] S. Yuasa, K. Kitagawa, T. Sakurazawa, I. Kumazawa, T. Sakurai, Liquid oxygen vaporization techniques for swirling-oxidizer-flow-type hybrid rocket engines, Int. J. Energ. Mater. Chem. Propuls. 10 (2) (2011) 155–168, <https://doi.org/10.1615/IntEnergMaterialsChemProp.2012001351>.
- [16] S. D. Eilers, S. Whitmore, Z. Peterson, US Patent No. US2014/0026537A1, 2014.
- [17] L. Kamps, S. Hirai, K. Sakurai, T. Viscor, Y. Saito, R. Guan, H. Isochi, N. Adachi, M. Itoh, H. Nagata, Investigation of graphite nozzle erosion in hybrid rockets using oxygen/high-density polyethylene, J. Propuls. Power 36 (2020) 423–434, <https://doi.org/10.2514/1.B37568>.
- [18] G. Gallo, L. Kamps, H. Shota, C. Carmicino, H. Nagata, One-dimensional modelling of the nozzle cooling with cryogenic oxygen flowing through helical channels in a hybrid rocket, Acta Astronaut. 210 (2023) 176–196, <https://doi.org/10.1016/j.actaastro.2023.05.013>.
- [19] G. Gallo, H. Kojima, L.T. Kamps, H. Nagata, Experimental investigation of regenerative cooling performance in hybrid rocket engines, Therm. Sci. Eng. Prog. 49 (2024) 102481, <https://doi.org/10.1016/j.tsep.2024.102481>.
- [20] C.T. Hendley, T.L. Connell Jr., D. Wilson, G. Young, Catalytic decomposition of nitrous oxide for use in hybrid rocket motors, J. Prop. Power 37 (2021) 474–478, <https://doi.org/10.2514/1.B38204>.
- [21] G. Gallo, L. Kamps, S. Hirai, C. Carmicino, H. Nagata, Prediction of the fuel regression-rate in a HDPE single port hybrid rocket fed by liquid nitrous oxide, Combust. Flame 259 (2024) 113160, <https://doi.org/10.1016/j.combustflame.2023.113160>.
- [22] G. Gallo, G.D. Di Martino, G. Festa, R. Savino, Experimental investigation of N<sub>2</sub>O decomposition with Pd/Al<sub>2</sub>O<sub>3</sub> cylindrical pellets catalyst, J. Spacecr. Rockets 57 (2020) 1–8, <https://doi.org/10.2514/1.A34700>.
- [23] A. Karabeyoglu, J. Dyer, J. Stevens, B. Cantwell, Modeling of N<sub>2</sub>O Decomposition Events, 44th AIAA/ASME/SAE/ASEE Joint Propulsion Conference & Exhibit, 2008, Hartford, United States, <http://arc.aiaa.org/10.2514/6.2008-4933>.
- [24] G.D. Di Martino, G. Gallo, S. Munguerra, G. Festa, R. Savino, Design and testing of a monopropellant thruster based on N<sub>2</sub>O decomposition in Pd/Al<sub>2</sub>O<sub>3</sub> pellets catalytic bed, Acta Astronaut. 180 (2021) 460–469, <https://doi.org/10.1016/j.actaastro.2020.12.016>.
- [25] L. Werling, T. Hörger, Experimental analysis of the heat fluxes during combustion of a N<sub>2</sub>O/C<sub>2</sub>H<sub>4</sub> premixed green propellant in a research rocket combustor, Acta Astronaut. 189 (2021) 437–451, <https://doi.org/10.1016/j.actaastro.2021.07.011>.
- [26] E. Browne, J. Rasmussen, A. Marchese, R. M. Zubrin, B. C. Windom, Modeling Single-Channel and Dual-Channel Regenerative Cooling Systems for an Ethylene/Ethane/Nitrous Oxide Liquid Fuel Rocket Engine, AIAA Scitech 2021 Forum, 2021, Virtual Event, United States, [Doi: 10.2514/6.2021-0049](https://doi.org/10.2514/6.2021-0049).
- [27] A. Kumara, V. Sainia, P. R. Usurumartib, R. S. Dondapatia, Feasibility Studies on the Cooling of Hybrid Rocket Nozzles.
- [28] P. Lemieux, Nitrous oxide cooling in hybrid rocket nozzles, Prog. Aerosp. Sci. 46 (2010) 106–115, <https://doi.org/10.1016/j.paerosci.2009.12.001>.

- [29] Anon., Isotropic Graphite: Typical Properties, [https://www.tokaicarbon.co.jp/en/products/fine\\_carbon/pdf/Isotropic\\_graphite.pdf](https://www.tokaicarbon.co.jp/en/products/fine_carbon/pdf/Isotropic_graphite.pdf).
- [30] W. Rasband, ImageJ, U.S. National Institutes of Health, Bethesda, MD, 1997.
- [31] A.I. Lutcov, V.I. Volga, B.K. Dymov, Thermal conductivity, electric resistivity and specific heat of dense graphite, *Carbon* 8 (1970) 753–760, [https://doi.org/10.1016/0008-6223\(70\)90100-4](https://doi.org/10.1016/0008-6223(70)90100-4).
- [32] H.H. Ku, Notes on the use of propagation of error formulas, *J. Res. Natl. Bur. Stand.* 70C (1966) 263–273, <https://doi.org/10.6028/jres.070C.025>.
- [33] D.R. Bartz, A simple equation for rapid estimation of rocket nozzle convective heat transfer coefficient, *Jet Propuls.* 27 (1957) 49–51.
- [34] P.A. Kew, K. Cornwell, Correlations for the prediction of boiling heat transfer in small-diameter channels, *Appl. Therm. Eng.* 17 (1997) 705–715, [https://doi.org/10.1016/S1359-4311\(96\)00071-3](https://doi.org/10.1016/S1359-4311(96)00071-3).
- [35] M. Matkovic, A. Cavallini, D. Del Col, L. Rossetto, Experimental study on condensation heat transfer inside a single circular minichannel, *Int. J. Heat Mass Transf.* 52 (9–10) (2009) 2311–2323, <https://doi.org/10.1016/j.ijheatmasstransfer.2008.11.013>.
- [36] Y. Qiu, T. Vo, D. Garg, H. Lee, C.R. Kharangate, A systematic approach to optimization of ann model parameters to predict flow boiling heat transfer coefficient in mini/micro-channel heatsinks, *Int. J. Heat Mass Transf.* 202 (2023) 123728, <https://doi.org/10.1016/j.ijheatmasstransfer.2022.123728>.
- [37] S. Kim, S.J. Darges, J. Hartwig, I. Mudawar, Assessment and development of saturated and subcooled heat transfer coefficient correlations for cryogenic flow boiling in tubes, *Int. J. Heat Mass Tran.* 224 (2024) 125297, <https://doi.org/10.1016/j.ijheatmasstransfer.2024.125297>.
- [38] V. Ganesan, R. Patel, J. Hartwig, I. Mudawar, Review of databases and correlations for saturated flow boiling heat transfer coefficient for cryogens in uniformly heated tubes, and development of new consolidated database and universal correlations, *Int. J. Heat Mass Tran.* 179 (2021) 121656, <https://doi.org/10.1016/j.ijheatmasstransfer.2021.121656>.